
A Formulation of Consistent Particle Hydrodynamics in Strong Form

Satoko YAMAMOTO^{1,2,3} and Junichiro MAKINO,^{3,2,1}

¹Department of Earth & Planetary Sciences, Tokyo Institute of Technology, 2-12-1, Ookayama, Meguro-ku, Tokyo 152-8550, Japan

²RIKEN Advanced Institute for Computational Science, 7-1-26, Minatojima-minamimachi, Chuo-ku, Kobe, Hyogo 650-0047, Japan

³Department of Planetology, Kobe University, 1-1, Rokkodaicho, Nada-ku, Kobe, Hyogo 650-0013, Japan

*E-mail: yamamoto.s.an@geo.titech.ac.jp

Received 0 0; Accepted 0 0

Abstract

In fluid dynamical simulations in astrophysics, large deformations are common and surface tracking is sometimes necessary. Smoothed Particle Hydrodynamics (SPH) method has been used in many of such simulations. Recently, however, it has been shown that SPH cannot handle contact discontinuities or free surfaces accurately. There are several reasons for this problem. The first one is that SPH requires that the density is continuous and differentiable. The second one is that SPH does not have the consistency, and thus the accuracy is zeroth order in space. In addition, we cannot express accurate boundary conditions with SPH. In this paper, we propose a novel, high-order scheme for particle-based hydrodynamics of compressible fluid. Our method is based on kernel-weighted high-order fitting polynomial for intensive variables. With this approach, we can construct a scheme which solves all of the three problems described above. For shock capturing, we use a tensor form of von-Neumann-Richtmyer artificial viscosity. We have applied our method to many test problems and obtained excellent result. Our method is not conservative, since particles do not have mass or energy, but only their densities. However, because of the Lagrangian nature of our scheme, the violation of the conservation laws turned out to be small. We name this method Consistent Particle

1 Introduction

In fluid dynamical simulations in astrophysics, large deformations are common and surface tracking is sometimes necessary. Mesh-free methods, in which particles move following the motion of fluid, are very useful for such simulations. In particular, Smoothed Particle Hydrodynamics (SPH; Lucy 1977, Gingold & Monaghan 1977) has been widely used in astrophysics and also in computer-aided engineering.

SPH is one of Lagrangian methods. In SPH, we assume that the fluid equation can be expressed by interactions between fluid particles. Therefore, SPH is not only suitable for simulation of large deformations, but also can satisfy the conservation laws.

Recently, however, it has become known that SPH has several difficulties. For example, it cannot handle contact discontinuities (e.g. Okamoto et al. 2003, Agertz et al. 2007) or fluid surfaces. In our opinion, the standard formation of SPH has the following three problems, 1) The density distribution must be differentiable (e.g. Saitoh & Makino 2013). Hence, SPH cannot handle the contact discontinuity properly. 2) Since the approximation of quantities in SPH is of zeroth order in space, SPH does not have the consistency to the original partial differential equation (e.g. Liu et al. 1995). According to the Lax equivalence theorem (Lax & Richtmyer 1956), a method, which does not have the consistency, does not converge to the original partial differential equation in the limit of the infinite resolution. 3) There is no mathematically sound way to specify boundary conditions in SPH, except for the mirror boundary condition. Traditionally, fixed particles have been used to express reflecting boundaries such as walls and bottom of a well. They are necessary because SPH cannot express a sharp cutoff in the density distribution. However, there is no way to let these fixed particles change their physical quantities correctly. Thus, smoothed estimate of physical quantities of particles near the boundary contains large errors.

To solve problem one, Ritchie & Thomas (2001), Ott & Schnetter (2003), Saitoh & Makino (2013) and Yamamoto et al. (2015) proposed modified formulation of SPH in which the differentiability of the density is not required. Their methods can handle the density discontinuity better than standard SPH (hereafter SSPH) does.

In previous studies, high-order scheme have been proposed as the solution to problem two.

Dilts (1999) formulated Moving Least Squares Particles Hydrodynamics (MLSPH) based on the Moving Least Square (MLS) technique. In Reproducing Kernel Particle Method (RKPM; Liu et al. 1995), the formulation is not MLS, but is similar. These methods were applied to inviscid fluid dynamics simulations. However, they have not been applied to large deformations. Corrective SPH Method (CSPM; Chen et al. 1999a, Chen et al. 1999b, Chen et al. 1999c, Chen & Beraun 2000) is based on the Taylor expansion and Method of Weighted Residuals (MWR). They calculated Burgers equation, conduction of heat, linear elastodynamics and others with CPHM. In addition, Zhang & Batra (2004) modified this scheme and they called it Modified SPH (MSPH). MSPH was applied to the elastic wave and the diffusion equation. For non-compressible fluid, Tamai et al. (2013) introduced high-order formulation into Moving Particle Semi-implicit method (Koshizuka & Oka 1996). In addition, Finite Particle Method (FPM; Liu et al. 2005) was developed using MWR to handle viscous fluid. They calculated dam break test with FPM. Corrected SPH (CSPH) in Staroszczyk (2010) successfully handled the dam break test of inviscid fluid by re-fitting the density frequently. The frequent re-fitting generates numerical viscosity, and particles move to reduce the number-density deviation. Thus, large viscosity occurs in their simulation. In other word, if fluid particles do not move following fluid line to prevent the number-density deviation, large numerical viscosity is induced.

There seems to be no high-order scheme without large numerical viscosity for inviscid fluid tested with the calculation of large deformations. Frontiere et al. (2016) argued that it is difficult to handle large deformations with a high-order scheme. Figure 1 shows the result of a simulation of the Kelvin-Helmholtz instability performed using the high-order mesh-free method presented in section 2.1. The simulation time is $t = 0.23\tau_{KH}$, where τ_{KH} is the time scale of the Kelvin-Helmholtz instability. We can see large deviations of the number-density of particles. These deviations are the result of the fact that each particle move following the fluid motion at its location accurately. Small-scale vortex can easily generate highly disordered distribution of particles. This problem is mathematically same as the generation of large density fluctuation in cold Keplerian disk (e.g. Imaeda & Inutsuka 2002). From the above, it is necessary to rearrange particles, when the large number-density deviation occurs.

One potential problem of high-order method is that they do not completely satisfy the conservation law because particles do not have extensive variables (Fang 2009, Frontiere et al. 2016). To construct a high-order mesh-free method which satisfies the conservation laws, we must define fluid particles which have extensive variables. Hence, each particle must also have its volume. This volume has to be represented by some physical shape of the particle. If the mass of a particle is constant, its shape of the particle has to change following the fluid deformation. Consider an initially spherical particle in velocity field with a uniform shear. It will become elongated very soon, and thus

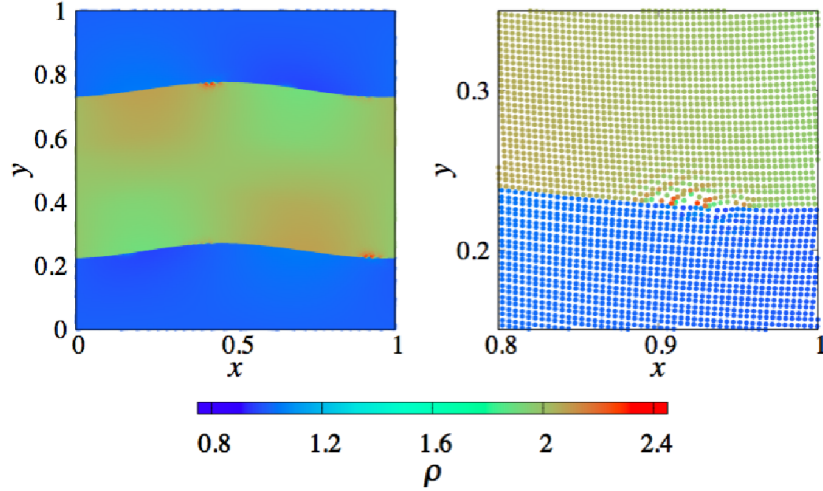


Fig. 1. The result of a simulation of the Kelvin-Helmholtz instability with our high-order method at $t = 0.23\tau_{\text{KH}}$. The right panel is the enlarge image of low-density region of the left.

numerical scheme would break down. Therefore, no high-order method can satisfy the conservation law completely. However, we found that the error of the conservation law is very small for high-order methods.

Concerning problem three, we can apply boundary conditions in mathematically meaningful and well-defined way because we approximate the partial differential equation using fitting polynomial for intensive variables in high-order mesh-free method.

We call our method Consistent Particle Hydrodynamics in Strong Form (CPHSF). We performed several numerical tests, and results were excellent.

In the rest of this paper, we present CPHSF (section 2), and report the results of numerical tests (section 3). Finally, we discuss and summarize our study (section 4).

2 The CPHSF scheme

As described in introduction, many different high-order approximation methods have been proposed in previous studies. In the following, we call these approximation methods "shape functions", since they can be written as

$$\hat{f}_{x,\dots,y,\dots,z,\dots}|_{\mathbf{r}=\mathbf{r}_i} \equiv \sum_j f_j \mathcal{W}_j(\mathbf{r}_j - \mathbf{r}), \quad (1)$$

where $\hat{f}_{x,\dots,y,\dots,z,\dots}$ is the approximation of a spacial partial derivative of function f with respect to variables $x, \dots, y, \dots, z, \dots$ at position \mathbf{r} , f_j is the value of function f at the location of particle j , \mathbf{r}_j ,

and \mathcal{W}_j is the "shape function" of particle j . These shape function can be classified by whether or not they are defined as the minimum of the L2 norm of the residual of the fitting. We call shape functions based on the minimization of L2 norm type 1 and others type 2.

2.1 Type 1 shape functions

In this section, we consider an approximation of function f , $\hat{f}(\mathbf{r})$, which minimizes

$$\epsilon = \sum_j \widetilde{W}_{ij} \left[\hat{f}(\mathbf{r}_j) - f_j \right]^2. \quad (2)$$

We assume $f(\mathbf{r})$ is of C^n class, i.e. $f(\mathbf{r})$ is n -times differentiable. Here, \widetilde{W}_{ij} is the weight of particle j for approximation at particle i .

To derive shape functions in the way similar to those in Staroszczyk (2010) and Tamai et al. (2013), we define

$$\hat{f}(\mathbf{r}_j) = \mathbf{p}_{ij} \cdot \boldsymbol{\delta} f(\mathbf{r})|_{\mathbf{r}=\mathbf{r}_i}, \quad (3)$$

$$\mathbf{p}_{ij} = (1, r_{1,j} - r_{1,i}, r_{2,j} - r_{2,i}, \dots, r_{d,j} - r_{d,i}, (r_{1,j} - r_{1,i})^2, (r_{1,j} - r_{1,i})(r_{2,j} - r_{2,i}), \dots, (r_{1,j} - r_{1,i})^n, (r_{1,j} - r_{1,i})^{n-1}(r_{2,j} - r_{2,i}), \dots, (r_{d,j} - r_{d,i})^n)^T, \quad (4)$$

$$\boldsymbol{\delta} = \left(\hat{1}, \frac{\hat{\partial}}{\hat{\partial}r_1}, \dots, \frac{\hat{\partial}}{\hat{\partial}r_d}, \dots, \frac{1}{n!} \frac{\hat{\partial}^n}{\hat{\partial}r_1^n}, \frac{1}{(n-1)!1!} \frac{\hat{\partial}^n}{\hat{\partial}r_1^{n-1}\hat{\partial}r_2}, \dots, \frac{1}{n!} \frac{\hat{\partial}^n}{\hat{\partial}r_d^n} \right)^T, \quad (5)$$

where $\hat{1}, \hat{\partial}^m / \hat{\partial}r^m$ are the approximations of $1, \partial^m / \partial r^m$ and have the error $\mathcal{O}(\|\mathbf{r}\|^{n+1-m})$, and d is the dimension of the space. Therefore, the right hand side of equation (3) matches the Taylor expansion around $\mathbf{r}_j = \mathbf{r}_i$ of $f(\mathbf{r}_j)$ up to for $(n - m)$ -th order for m -th order spatial derivatives.

If we do not need the interpolation formula for f_i , it is possible to set $\hat{1} = 1$ (e.g. Tamai et al. 2013). However, in this paper, we need the interpolation formula for f_i in section 2.4. Therefore, we do not use this form.

The optimal $\boldsymbol{\delta} f(\mathbf{r})|_{\mathbf{r}=\mathbf{r}_i}$ for which ϵ takes the extreme, is given by

$$\boldsymbol{\delta} f(\mathbf{r})|_{\mathbf{r}=\mathbf{r}_i} = B_i^{-1} \sum_j \widetilde{W}_{ij} f_j \mathbf{p}_{ij}, \quad (6)$$

$$B_i = \sum_j \widetilde{W}_{ij} \mathbf{p}_{ij} \otimes \mathbf{p}_{ij}, \quad (7)$$

where B_i is a regular matrix. Note that if B_i becomes a rank deficient, it means that the set of f_j does not have enough information to derive a unique $\boldsymbol{\delta} f(\mathbf{r})|_{\mathbf{r}=\mathbf{r}_i}$. Therefore, in such a case, we widen the non-zero region of \widetilde{W}_{ij} to increase the number of particles in the shape function.

In this paper, we set $\widetilde{W}_{ij} = W_{ij}$, where W_{ij} is a kernel function that depends on \mathbf{r}_{ij} and h_i . Here, h_i is a kernel length that denotes the width of the kernel function. In SPH, it is usually given by

$$h_i = \eta \left(\frac{m_i}{\rho_i} \right)^{1/d}, \quad (8)$$

where η is a constant coefficient. The parameters m and ρ are the mass and the mass-density.

From the above, the contribution of f_j to $\hat{f}(\mathbf{r}_i)$ is given by

$$\phi_{ij} = \sum_{\alpha} [B_i^{-1}]_{0\alpha} W_{ij} p_{\alpha,ij}, \quad (9)$$

and that to derivatives $\partial/\partial \mathbf{r}_{\beta} [\hat{f}(\mathbf{r}_i)]$ is

$$\psi_{\beta,ij} = \sum_{\alpha} [B_i^{-1}]_{\beta\alpha} W_{ij} p_{\alpha,ij}, \quad (10)$$

where $[B_i]_{\alpha\beta}$ is element α, β of matrix B_i and $p_{\alpha,ij}$ is element α of vector \mathbf{p}_{ij} . Note that index β takes $1 \leq \beta \leq d$ in equation (10).

Alternatively, in MLSPH, the derivative of equation (9) is used as $\partial/\partial \mathbf{r}_{\beta} [\hat{f}(\mathbf{r}_i)]$. In this case, all components of $\delta f(\mathbf{r})|_{\mathbf{r}=\mathbf{r}_i}$ are freely changed to minimize the residual. Therefore, the error is smaller than that of equation (10). However, we can get only zeroth order differential shape function, and thus it takes calculation cost to differentiate shape function which consists of a matrix and others. Therefore, we use equation (10) as a differential shape function.

In this paper, we define that the scheme is n -th order in space, if the first-order spatial derivative is n -th order.

2.2 Type 2 shape functions

We derived the shape functions using MLS in section 2.1. However, the shape functions of CSPM, MSPH and FPM cannot be expressed in terms of MLS because these functions are derived from the idea different from MLS. In this section, we derive them using MWR. In MWR, the weighted approximation error is set zero.

$$\int [f_j - \hat{f}(\mathbf{r}_j)] \widehat{W}_{ij} d\mathbf{r}_j = 0. \quad (11)$$

In this section, we show that the shape functions of CPHM, MSPH and FPM can be derived using the trial function of the form in equation (3). Here, since there are ${}_{(d+n)}C_d$ unknown parameters, we need to give ${}_{(d+n)}C_d$ differential forms of \widehat{W}_{ij} . In these methods, these functions are given by

$$\begin{aligned} \mathbf{q}_{ij}^t = & (W_{ij}, \nabla_1 W_{ij}, \nabla_2 W_{ij}, \dots, \nabla_d W_{ij}, \nabla_1^2 W_{ij}, \nabla_1 \nabla_2 W_{ij}, \\ & \dots, \nabla_1^n W_{ij}, \nabla_1^{n-1} \nabla_2 W_{ij}, \dots, \nabla_d^n W_{ij}), \end{aligned} \quad (12)$$

Thus, we have

$$\int [f_j - \hat{f}(\mathbf{r}_j)] \mathbf{q}_{ij} d\mathbf{r}_j = 0. \quad (13)$$

Note that the n -th order differential shape functions in CSPM are derived recursively by using zero to $(n - 1)$ order derivatives. Therefore, $\hat{f}(\mathbf{r}_i)$ is given by setting $\mathbf{q}_{ij}^t = W_{ij}$, and then the first derivatives are produced by using this $\hat{f}(\mathbf{r}_i)$ and setting $\mathbf{q}_{ij}^t = (\nabla_1 W_{ij}, \nabla_2 W_{ij}, \dots, \nabla_d W_{ij})$.

Finally, the integral $\int f_j d\mathbf{r}_j$ is approximated by summation $\sum_j f_j V_j$, and we have

$$\delta f_i = B_i'^{-1} \sum_j f_j V_j \mathbf{p}_{ij}, \quad (14)$$

$$B_i' = \sum_j V_j \mathbf{p}_{ij} \otimes \mathbf{q}_{ij}, \quad (15)$$

where V_j is the ‘‘volume’’ of particle j . From the above, the contribution of f_j to $\hat{f}(\mathbf{r}_i)$ is given by

$$\phi'_{ij} = \sum_{\alpha} [B_i'^{-1}]_{0\alpha} V_j p_{\alpha,ij}, \quad (16)$$

and that of derivatives $\partial/\partial \mathbf{r}_{\beta} \hat{f}(\mathbf{r}_i)$ is

$$\psi'_{\beta,ij} = \sum_{\alpha} [B_i'^{-1}]_{\beta\alpha} V_j p_{\alpha,ij}. \quad (17)$$

In the following, we use the shape functions of equations (9) and (10).

2.3 The artificial viscosity for multi-dimensions

Many forms of the artificial viscosity have been proposed for SPH to capture shocks (e.g. Lattanzio et al. 1985, Monaghan 1997). However, most of them cause unwanted shear viscosity (e.g. Balsara 1995, Cullen & Dehnen 2010).

To reduce unwanted shear viscosity, Balsara (1995) and Cullen & Dehnen (2010) introduced shear switches that reduce viscosity when the shear exists. Alternatively, Inutsuka (2002) and Hopkins (2015) proposed the use of Riemann solvers in order not to use the artificial viscosity. Hernquist & Katz (1989) introduced a form of the artificial viscosity different from that of Monaghan & Gingold (1983). This artificial viscosity (hereafter NRAV) was derived by adding the bulk viscosity to the artificial viscosity formulated by von Neumann & Richtmyer (1950). This viscosity is applied only when $\nabla \cdot \mathbf{v} < 0$, where \mathbf{v} is the velocity. Hosono et al. (2016) compared many different forms of artificial viscosities, including the usual Monaghan & Gingold (1983) type, and NR type, both with and without different forms of shear switches and time-dependent switches. They found the NR type viscosity is the best, when the estimate of $\nabla \cdot \mathbf{v}$ is of high order. When a low-order estimate is used, it causes unwanted shear viscosity.

These proposed forms of the artificial viscosity can handle fluid with the velocity shear better than the standard artificial viscosity of SPH can. The standard SPH artificial viscosity is defined for pairs of particles, and thus there is no easy way to apply it to high-order schemes in which particles

do not have extensive quantities. Moreover, Hosono et al. (2016) demonstrated that even for SPH schemes, NRAV is better than the standard SPH artificial viscosity. Therefore, we adopted NRAV. Initially, we used the usual form of NRAV extended to multi-dimensional space

$$\frac{d\mathbf{v}}{dt} = -\frac{1}{\rho} \frac{\partial q^{\text{AV}}}{\partial \mathbf{r}}, \quad (18)$$

$$\frac{du}{dt} = -\frac{q^{\text{AV}}}{\rho} \frac{\partial \mathbf{v}}{\partial \mathbf{r}}, \quad (19)$$

$$q^{\text{AV}} = -\beta^{\text{AV}} \rho h^2 \frac{\partial \mathbf{v}}{\partial \mathbf{r}} \cdot \left| \frac{\partial \mathbf{v}}{\partial \mathbf{r}} \right| \Theta(-\partial \mathbf{v} / \partial \mathbf{r}), \quad (20)$$

where β^{AV} is a constant coefficient and u is the internal energy. The function $\Theta(\chi)$ is the Theta function. We, however, found that this form leads to numerical instability. The reason why the instability takes place is that the pressure-like quantity in NRAV in equations (18) and (19) is isotropic. Therefore, these “pressure” can and does operate to directions perpendicular to the direction of compression, resulting in the increase of the kinetic energy. Therefore, we extend the NRAV to multi-dimensions so that the artificial viscosity operates only in the direction of the maximum compression. Note that we assume that the number of shock waves at one position is only one.

Let X the coordinate of the direction of a shock wave. von Neumann & Richtmyer (1950) introduced the following the artificial viscosity to equations of moment and energy.

$$\frac{dv_X}{dt} = -\frac{1}{\rho} \frac{\partial q^{\text{AV}}}{\partial X}, \quad (21)$$

$$\frac{du}{dt} = -\frac{q^{\text{AV}}}{\rho} \frac{\partial v_X}{\partial X}, \quad (22)$$

$$q^{\text{AV}} = -\beta^{\text{AV}} \rho h^2 \frac{\partial v_X}{\partial X} \cdot \left| \frac{\partial v_X}{\partial X} \right| \Theta(-\partial v_X / \partial X). \quad (23)$$

To extend this artificial viscosity to multi-dimensions, first, we determine the direction of X axis along which the fluid is maximally compressed. Second, the artificial viscosity for this X -direction is calculated. Finally, we transform the calculated the artificial viscosity into the original system of coordinates. The strain rate tensor is given by

$$s_{\alpha\beta} = \frac{1}{2} \left(\frac{\partial v_\alpha}{\partial r_\beta} + \frac{\partial v_\beta}{\partial r_\alpha} \right). \quad (24)$$

Using eigenvalues $\lambda_1, \dots, \lambda_d$ and eigenvectors $\mathbf{b}_1, \dots, \mathbf{b}_d$, s is diagonalized as

$$\begin{pmatrix} \lambda_1 & 0 & \dots & 0 \\ 0 & \ddots & \ddots & 0 \\ \vdots & \ddots & \ddots & 0 \\ 0 & \dots & 0 & \lambda_n \end{pmatrix} = (\mathbf{b}_1, \dots, \mathbf{b}_d)^t s (\mathbf{b}_1, \dots, \mathbf{b}_d), \quad (25)$$

We assume eigenvalues are ordered, $\lambda_1 \leq \lambda_2 \leq \dots \leq \lambda_d$. Thus, if $\nabla \cdot \mathbf{v} < 0$, we apply the artificial

viscosity in the direction of \mathbf{b}_1 . Here, the transformed coordinate is given by

$$\mathbf{r}' = \mathbf{r}(\mathbf{b}_1, \mathbf{b}_2, \dots, \mathbf{b}_d). \quad (26)$$

First, we derive the artificial viscosity in the equation of motion. In the transformed coordinate, the artificial viscosity term is given by

$$\frac{d\mathbf{v}'}{dt} = \left(\frac{1}{\rho} \frac{\partial q'}{\partial r'_1}, 0, \dots, 0 \right), \quad (27)$$

$$q'^{\text{AV}} = -\beta^{\text{AV}} \rho h^2 \lambda_1 |\lambda_1| \Theta(-\nabla \cdot \mathbf{v}). \quad (28)$$

Therefore, in the original coordinate, the artificial viscosity term in the equation of motion is

$$\frac{d\mathbf{v}}{dt} = \left(\frac{1}{\rho} \frac{\partial q'}{\partial r'_1}, 0, \dots, 0 \right) (\mathbf{b}_1, \mathbf{b}_2, \dots, \mathbf{b}_d). \quad (29)$$

Here, by using the quantities in the original coordinate, $\partial q' / \partial r'_1$ can be expressed by

$$\frac{\partial q'}{\partial r'_1} = \frac{\partial q'}{\partial \mathbf{r}} \cdot \mathbf{b}_1. \quad (30)$$

From the above, the artificial viscosity term in the equation of motion in the original coordinate is given by

$$\frac{d\mathbf{v}}{dt} = -\mathbf{b}'_1 \frac{1}{\rho} \frac{\partial q'^{\text{AV}}}{\partial \mathbf{r}} \cdot \mathbf{b}_1, \quad (31)$$

where \mathbf{b}'_1 is $(b_{1,1}, b_{2,1}, \dots, b_{n,1})$. Here, $b_{\alpha,1}$ denotes the first element of \mathbf{b}_α . Next, we derive the artificial viscosity in the equation of energy. In this case, it is the same artificial viscosity for both the original coordinate and the transformed one because the equation of energy is scalar. Therefore,

$$\frac{du}{dt} = -\frac{q'^{\text{AV}}}{\rho} \lambda_1. \quad (32)$$

In this paper, we also use the bulk viscosity introduced by Monaghan & Gingold (1983). Therefore, q'^{AV} changes to

$$q'^{\text{AV}} = -[\alpha^{\text{AV}} \rho c_s h + \beta^{\text{AV}} \rho h^2 |\lambda_1|] \lambda_1 \Theta(-\nabla \cdot \mathbf{v}), \quad (33)$$

In this paper, we use $\alpha^{\text{AV}} = 1$ and $\beta^{\text{AV}} = 2$ where α^{AV} is a constant coefficient, and c_s is the sound velocity.

The introduction of the linear bulk viscosity of equation (33) implies that the viscosity is active even for infinitesimal compression. In other words, the fluid is viscous even if there is no shock. In order to reduce the viscosity in the absence of the shock, so-called ‘‘bulk switches’’ have been proposed (Morris & Monaghan 1997, Rosswog et al. 2000). We use the switch ζ multiplied to q'^{AV} . The time evolution of ζ is given by

$$\frac{d\zeta}{dt} = -(\zeta_{\max} - \zeta) \max(-\nabla \cdot \mathbf{v}, 0) - \frac{\zeta - \zeta_{\min}}{\tau_{\text{AV}}}, \quad (34)$$

$$\tau_{AV} = c_{\tau_{AV}} \frac{h}{c_s}, \quad (35)$$

where $c_{\tau_{AV}}$ is a parameter which determines the decay time scale of the artificial viscosity after shock. In this paper, we use $c_{\tau_{AV}} = 1$ and $\zeta_{\max} = 2$, following Rosswog et al. (2000) and Hosono et al. (2016). We discuss the choice of ζ_{\min} in section 3.2.

Finally, we introduce a new term which weakens the artificial viscosity when fluid is compressed in one direction, but is expanding in other directions,

$$F^{AV} = \left(\frac{|\sum_m \lambda_m|}{\sum_m |\lambda_m|} \right)^v, \quad (36)$$

where v is a positive coefficient. Consider the case that $|\lambda_1| = |\lambda_2|$ and $\lambda_1 + \lambda_2 = 0$. Obviously, $\nabla \cdot \mathbf{v} = 0$, and there is no compression. However, numerically determined $\nabla \cdot \mathbf{v}$ can be negative due to truncation errors and in that case equation (33) can result in the strong artificial viscosity. We can reduce this erratic activation of the artificial viscosity using this term. In this paper, we use $v = 2$. We multiply q'^{AV} by ζ and F^{AV} . Thus, in our study, we use

$$q^{AV} = \zeta F^{AV} q'^{AV}, \quad (37)$$

instead of q'^{AV} .

2.4 Rearrangement of particles

As we have discussed in section 1, the rearrangement of particles is necessary to handle large deformations of inviscid fluid, if we use high-order schemes. Therefore, in this section, we describe how to rearrange particles. In this paper, we consider two dimensional cases.

First, we consider periodic boundary. In this case, particles are rearranged to the initial pattern. Of course, the initial pattern does not have large deviations of the number density of particles. For example, consider the case in which initial pattern is a grid. If the distribution of particles has become distorted as in the left-hand side panel in figure 2, we rearrange particles in a grid pattern (see the right in figure 2).

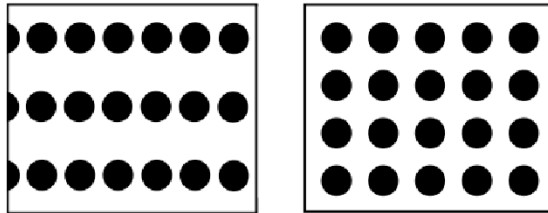


Fig. 2. An illustration of the rearrangement of particles. Particles in a distorted placement (left) is replaced by a regular placement (right).

Next, we consider the fluid with the surface. In this paper, particles are rearranged to the original grid pattern. Consider the case where particles are distributed as in the left-hand side panel of figure 3. First, we connect surface particles with lines which are expressed as black lines in the central panel of figure 3. Then, particles are placed on the intersections of the black line and the grid line, for example, the black dots in the central panel of figure 3. If the interval between particles is smaller than $0.81\Delta r_{\text{grid}}$, where Δr_{grid} is the width of a grid, one particle is removed. Finally, we put particles on grid points as in the right-hand side panel of figure 3.

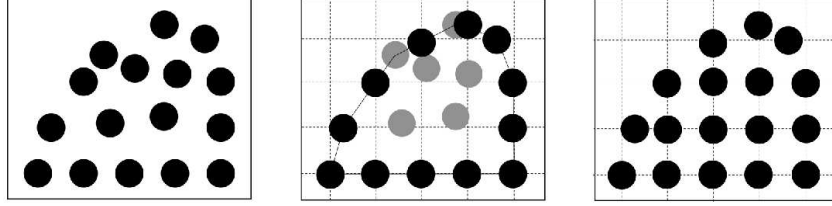


Fig. 3. An illustration of the rearrangement of particles on and near the surface. Particles in a distorted placement (left) is replaced by a regular placement (right). New particles on the surface are generated at the intersection of the surface and grid lines.

The physical quantity, f_i , of a new particle i is calculated by using f'_j , where f'_j is the quantity of particle j before rearrangement.

$$f_i = \sum_j f'_j \phi_{ij}. \quad (38)$$

Finally, we describe the criterion for rearrangement. Typically, rearrangement is required when local distribution of particles has become highly anisotropic. Consider a simple velocity field with linear shear, such as $v_x = -y$, applied to initial particle distribution of a tilted cartesian grid (see the left side panel of figure 4). Particles move through shear velocity and the distribution transforms to that given by the central panel of figure 4. Very soon, large difference between distance of particles in one direction and that in the orthogonal direction develops as shown in the right panel in figure 4.

In order to detect this kind of anisotropy, we use an approximate kernel weighted moment tensor defined as

$$I_i = \begin{pmatrix} \sum_j M_i(x_{ij})^2 W_{ij} & \sum_j M_i(x_{ij}) M_i(y_{ij}) W_{ij} \\ \sum_j M_i(x_{ij}) M_i(y_{ij}) W_{ij} & \sum_j M_i(y_{ij})^2 W_{ij} \end{pmatrix}, \quad (39)$$

$$M_i(\chi) = \text{sgn}(\chi) \left(1 - \frac{\chi}{H_i} \right), \quad (40)$$

where $\text{sgn}(\chi)$ is a sign function, and x_{ij} and y_{ij} are $(x_j - x_i)$ and $(y_j - y_i)$. The parameter H_i equal to the width of the kernel function W_{ij} . Therefore, if $|\chi|$ is larger than H_i , the value of W_{ij} is zero.

The criterion of the rearrangement is given by

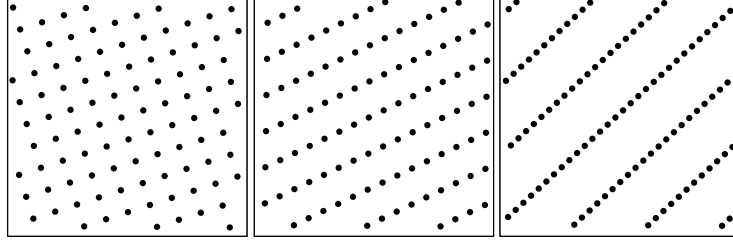


Fig. 4. The distortion of the distribution of particles initially in the rectangular grid (left) due to the velocity field of uniform shear. The center and right panels show the distribution of particles after the particles in the top and bottom edges move once and twice of the length of the edge.

$$\left| 1 - \frac{\Lambda_{\min}}{\Lambda_{\max}} \right| > c_{\text{rea}}, \quad (41)$$

where Λ_{\max} and Λ_{\min} are maximum and minimum eigenvalues of I_i , and c_{rea} is a constant coefficient. Note that it is difficult to apply this criterion to the fluid surface, since it lacks particles near the surface. Hence, we apply rearrangement at a constant time interval, when we need to follow the surface.

2.5 Fluid equations

In this section, we derive our high-order mesh-free fully Lagrangian discretization of equations of continuity, moment and energy. The original set of partial differential equations are given by

$$\frac{d\rho}{dt} = -\rho \nabla \cdot \mathbf{v}, \quad (42)$$

$$\frac{d\mathbf{v}}{dt} = -\frac{\nabla P}{\rho}, \quad (43)$$

$$\frac{du}{dt} = -\frac{P}{\rho} \nabla \cdot \mathbf{v}, \quad (44)$$

where P is pressure. These equations are discretized using equation (10), and the artificial viscosity is added. Hence, we have

$$\frac{d\rho_i}{dt} = -\rho_i \sum_j \mathbf{v}_j \cdot \boldsymbol{\psi}_{ij}, \quad (45)$$

$$\frac{d\mathbf{v}_i}{dt} = -\frac{1}{\rho_i} \sum_j [P_j \boldsymbol{\psi}_{ij} + (q_j^{\text{AV}} \boldsymbol{\psi}_{ij} \cdot \mathbf{b}_1) \mathbf{b}'_1], \quad (46)$$

$$\frac{du_i}{dt} = -\frac{1}{\rho_i} \sum_j (P_j \mathbf{v}_j \cdot \boldsymbol{\psi}_{ij} + q_j^{\text{AV}} \lambda_1). \quad (47)$$

If the fluid is an ideal gas, the equation of state is given by

$$P = (\gamma - 1)\rho u, \quad (48)$$

where γ is the ratio of specific heat. Following Monaghan (1994), we use the equation for the water given by

$$P = C_B \left[\left(\frac{\rho}{\rho_{\text{air}}} \right)^7 - 1 \right] + P_{\text{air}}, \quad (49)$$

where ρ_{air} and P_{air} are density and pressure at the surface. The constant coefficient C_B is

$$C_B = \frac{200|g|H\rho_{\text{air}}}{7}. \quad (50)$$

Here g is the gravitational acceleration and H is the height of a fluid. For a weakly compressible fluid, we use the linearized equation of state

$$P = c_0^2(\rho - \rho_{\text{air}}), \quad (51)$$

where $c_0 = 10\sqrt{|g|H}$.

Following Hernquist & Katz (1989) and Hosono et al. (2016), the timestep Δt is given by

$$\Delta t = \min_i C_{\text{CFL}} \frac{h_i}{h_i |\nabla \cdot \mathbf{v}_i| + c_{si} + 1.2 [\alpha^{\text{AV}} c_{si} - \beta^{\text{AV}} h_i \min(0, \nabla \cdot \mathbf{v}_i)]}. \quad (52)$$

We set the constant coefficient C_{CFL} to 0.3 unless we state otherwise.

The kernel length h_i is calculated as

$$h_i = \eta \left(\frac{\tilde{m}_i}{\rho_i} \right)^{1/d}, \quad (53)$$

$$\tilde{m}_i = \rho_{0,i} \prod_{l=1}^d \Delta r_{l,i}, \quad (54)$$

where Δr_i and $\rho_{0,i}$ are an initial or rearranged particle spacing and density. In this paper, we set η to 1.6, 2.2, 3.0 and 3.8 for first-, second-, third- and fourth-order fitting formulae in space.

2.6 Boundary condition

In our method, we can express boundary conditions directly, since our method is based on fitting polynomials for intensive variables. First, we consider a free surface. At the free surface, the pressure of the fluid is same as that of thin air or vacuum. Thus, the boundary condition is given by

$$P = P_0, \quad (55)$$

where P_0 is a constant pressure of the assumed air. Now let us consider a fixed slipping boundary. The boundary condition is

$$v_{\perp} = 0. \quad (56)$$

Here, v_{\perp} is the velocity perpendicular to the boundary. In the case of the non-slipping boundary, a fluid element should stay at its initial point. Therefore, for the non-slip fixed boundary, the boundary condition is

$$\mathbf{v} = \mathbf{0}. \quad (57)$$

Finally, at the slipping contact discontinuity, pressure and velocity perpendicular to the boundary are continuous. Thus, the boundary conditions of contact discontinuity of fluid 1 and 2 are

$$P_1 = P_2, \quad (58)$$

$$v_{1,\perp} = v_{2,\perp}, \quad (59)$$

where P_i and $v_{i,\perp}$ are pressure and velocity perpendicular to the discontinuity of the fluid i . The boundary conditions at the non-slipping contact discontinuity are given by

$$P_1 = P_2, \quad (60)$$

$$\mathbf{v}_1 = \mathbf{v}_2, \quad (61)$$

where \mathbf{v}_i is velocity of the fluid i .

3 Test calculations

In this section, we show the results of several numerical tests. First, we compare capabilities of CPHSF and SSPH to handle the fluid surface by calculating linearize sound modes in section 3.1. In section 3.2, the result of the Sod shock tube test is presented. Here we investigate the errors of the conservation laws. In section 3.3, we show the result of the rotating cone test. Kelvin-Helmholtz instability (section 3.4) and Rayleigh-Taylor instability (section 3.5) are also calculated. They are suitable to survey the capability to handle large deformations and fluid instability. In addition, we investigate if CPHSF can handle free surfaces by gravity wave test (section 3.6) and dam break test (section 3.7). Finally, a cold Keplerian disk is calculated in section 3.8. In these tests, we used the Backward Euler integrator for tests with boundary conditions, and we used a third-order Runge-Kutta method for other tests. For shape functions, we used the first-order shape function in space unless stated otherwise. The kernel function is the fourth-order Wendland function (Wendland 1995).

3.1 The one-dimensional behavior of fluid with free surface

In this section, we investigate how SSPH and CPHSF handle the fluid surface by analyzing one-dimensional sound wave modes. We assume the fluid is water with equation of state given by equation (49) with $P_{\text{air}} = 0$ and $\rho_{\text{air}} = 1000$. The position, velocity, density and pressure of particle i in the

equilibrium are given by x_i , v_0 , ρ_0 and P_0 . In addition, perturbations are δx_i , δv_i , $\delta \rho_i$ and δP_i . The computational domain is $0 \leq x \leq 1$. The number of particles is 101. The values of v_0 , ρ_0 and P_0 are 0, 1000 and 0 for all i .

3.1.1 Standard SPH

First, we derive the linearized equation of the density perturbation in SSPH. The fluid equation of SSPH is given by

$$\frac{dx_i}{dt} = v_i, \quad (62)$$

$$\rho_i = \sum_j m_j W_{ij}, \quad (63)$$

$$\frac{dv_i}{dt} = - \sum_j m_j \left(\frac{P_j}{\rho_j^2} + \frac{P_i}{\rho_i^2} \right) \nabla W_{ij}. \quad (64)$$

Note that the value of ρ_i given by equation (63) does not become 1000 because the approximation has zeroth-order error. Therefore, we derive m_i , which satisfies $\rho_i = 1000$ for all i , by implicitly calculating the following equation,

$$1000 = \sum_j m_j W_{ij}. \quad (65)$$

Alternatively, we could adjust the locations of particles so that equation (65) is satisfied for equal-mass particles, but we chose to change mass for simplicity. In this test, mass distribution becomes as figure 5.

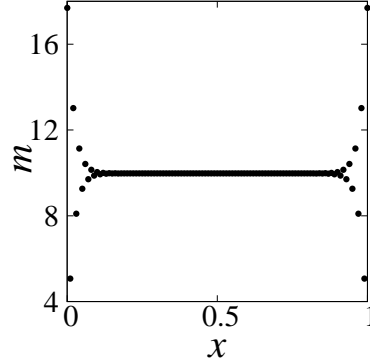


Fig. 5. Mass distribution which satisfies equation (65) with the equal particle spacing.

The perturbation equation for equations (62) to (64) is given by

$$\frac{d^2 \delta \rho_i}{dt^2} = \frac{c_{s0}^2}{\rho_0^2} \sum_j \sum_k m_j m_k \left(-\nabla W_{jk} (\nabla W_{ik} - \nabla W_{ij}) \delta \rho_j - \nabla W_{ik} \nabla W_{ij} (\delta \rho_j + \delta \rho_i) \right),$$

(66)

where c_{s0} is the sound velocity of the equilibrium state.

3.1.2 CPHSF

We derive the linearized equation of the density perturbation in CPHSF. The fluid equation of CPHSF is given by equations (45), (46) and (47). The linearized perturbation equation is given by

$$\frac{d^2 \delta \rho_i}{dt^2} = c_{s0}^2 \sum_j \sum_k \delta \rho_k \psi_{jk} \psi_{ij}. \quad (67)$$

Equation (55) is used for the boundary condition. Therefore the value of $\delta \rho_i$ is set zero at $x_i = 0, L$, where L is the width of the fluid and equal 1 in this test.

We used CPHSF of first- and third-order in space.

3.1.3 Exact solution

The perturbation equation at the continuous limit is the wave equation,

$$\frac{d^2 \delta \rho}{dt^2} = c_{s0}^2 \nabla^2 \delta \rho. \quad (68)$$

The boundary condition is $\delta \rho = 0$ at $x = 0$ and $x = L$ as that of CPHSF. Consequently, the general solution is given by

$$\delta \rho = \sum_k A(k) \sin\left(\frac{2\pi k}{L} x\right) e^{\omega t} \quad k \in \mathbb{N}, \quad (69)$$

$$\omega = i c_{s0} \frac{2\pi k}{L}, \quad (70)$$

where $A(k)$ is the amplitude of mode with wave number k .

3.1.4 Results

Figure 6 shows the eigenvalues of the modes as function of wave number k . We can see that the third-order CPHSF gives very accurate angular frequency even for large wave numbers. The first-order CPHSF and standard SPH give similar errors. Figure 7 shows the eigenfunctions of $k = 6$, and figure 8 gives the error of eigenfunctions. From these figures, we can see that the error of eigenfunction calculated with CPHSF is much smaller than that with SSPH, even when the spatial order of CPHSF is one.

We can conclude that CPHSF is more accurate than SSPH, in particular near the boundary, even when the spatial order is low.

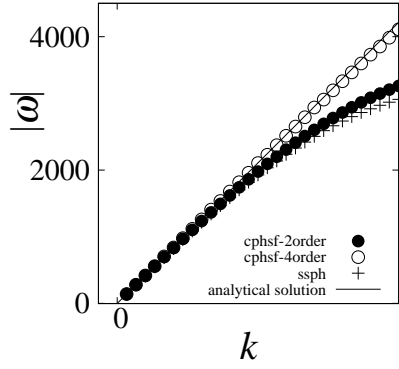


Fig. 6. The absolute value of the frequency ω plotted against the number of the wave k for SSPH and first and third space-order CPHSF.

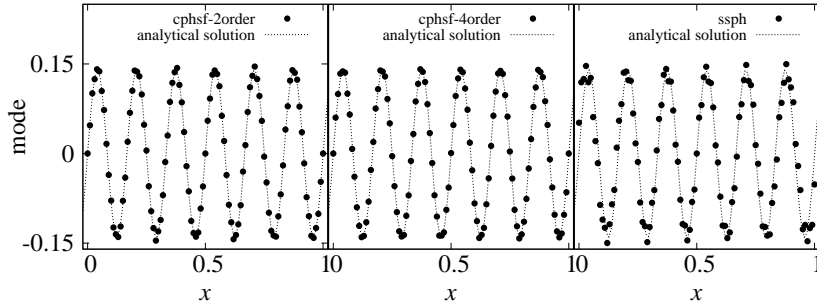


Fig. 7. The eigenfunction for $k = 6$. The left and central panels are for CPHSF with first- and third-order in space. The right is for SSPH.

3.2 Sod shock tube test

In this section, we present the result of the Sod shock tube test (Sod 1978). First, we determine the value of ζ_{\min} so that after-shock numerical oscillation is suppressed. Second, we investigate the errors of conserved quantities. We assume that fluid is ideal gas with $\gamma = 1.4$.

The computational domain is $-0.5 \leq x < 0.5$ with a periodic boundary condition, and the initial boundary of two fluids is at $x = -0.5, 0$. In this test, we use equal-mass particles. The numbers of particles are 800 (high density region) and 200 (low density region), and the total number of particles is 1000. Initial velocity is given by $v_x = 0$. The density is smoothed by a polynomial, and it is given by

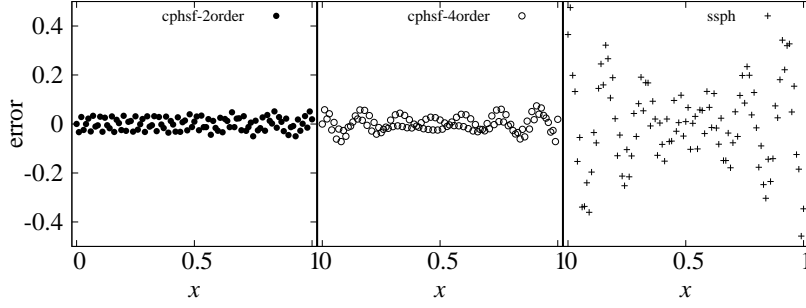


Fig. 8. The same as figure 7 but show the errors of eigenfunctions.

$$\rho(x) = \begin{cases} \rho_h, & -0.5 + x_0 \leq x < -x_0 \\ \rho_l, & x_0 \leq x < 0.5 - x_0 \\ \frac{\rho_h - \rho_l}{4} \left[\left(\frac{x}{x_0} \right)^3 - \frac{3x}{x_0} \right] + \frac{\rho_h + \rho_l}{2}, & \text{otherwise} \end{cases} \quad (71)$$

where ρ_h and ρ_l are the initial density of the high- and low-density regions. We used $\rho_h = 1$ and $\rho_l = 0.25$. The parameter x_0 represents the width of the smoothing region, and the value is given by $x_0 = 0.6(h_h + h_l)$, where h_h and h_l are the kernel length in the high- and low-density regions. The position of particle i in the smoothing region is determined so that they satisfy

$$\int_{x_{i-1}}^{x_i} \rho(x) dx = \tilde{m}_i. \quad (72)$$

The smoothed pressure is given by

$$P(x) = \begin{cases} P_h, & -0.5 + x_0 \leq x < -x_0 \\ P_l, & x_0 \leq x < 0.5 - x_0 \\ \frac{P_h - P_l}{4} \left[\left(\frac{x}{x_0} \right)^3 - \frac{3x}{x_0} \right] + \frac{P_h + P_l}{2}, & \text{otherwise} \end{cases} \quad (73)$$

where P_h and P_l are the initial pressure of the high- and low-density regions. We used $P_h = 1$ and $P_l = 0.1795$.

Figure 9 shows the numerical solution at $t = 0.1$ with first-order CPHSF with $\zeta_{\min} = 0.1$. The post shock oscillation is rather strong. Figure 10 shows the numerical solution for $\zeta_{\min} = 0.5$. In this figure, the post shock oscillation is suppressed. We use $\zeta_{\min} = 0.5$ for other tests in this paper unless stated otherwise.

We now investigate the errors in conserved quantities. We used first- and third-order schemes. We set $\zeta = 1$ in these tests. In the following, we report the result of two series of test calculations. We varied the number of particles from $N = 1000$ to 8000 for one test and from $N = 1000$ to 16000

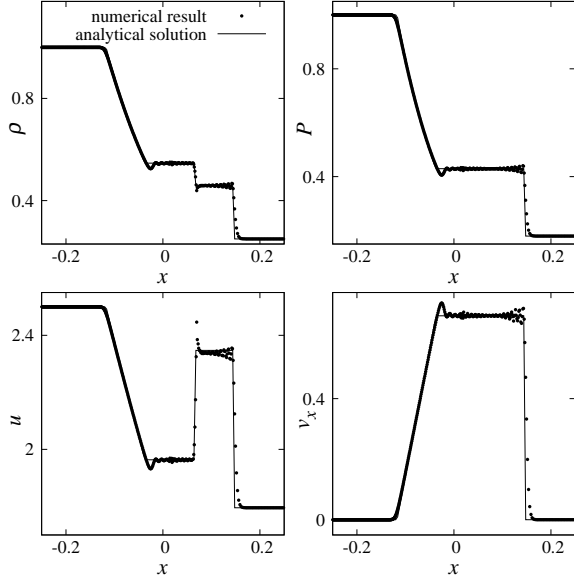


Fig. 9. Result of the Sod shock tube test at $t = 0.1$ with first-order CPHSF. We used $\zeta_{\min} = 0.1$.

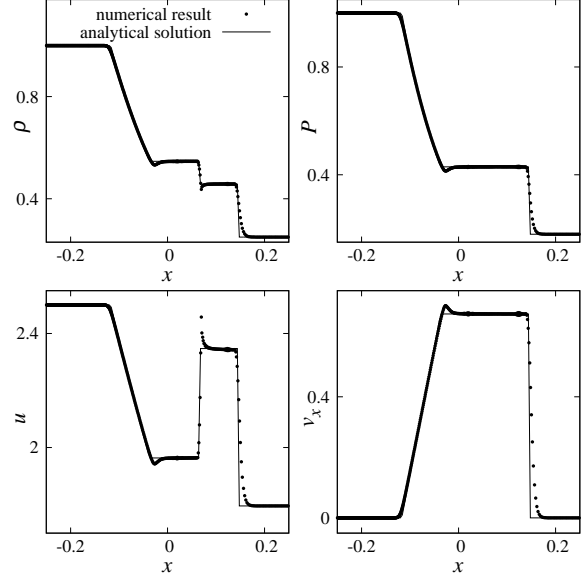


Fig. 10. The same as figure 9, but for $\zeta_{\min} = 0.5$.

for the other. The kernel length is calculated using equations (53) and (54). In the first series, we used the NRAV of the form described in section 2.3. This means that the strength of AV is weaker for higher resolution, so that the number of particles used to resolve shock is approximately constant. In the second series, we fixed the value of h for equation (33) and initial smoothing parameter x_0 in equations (71) and (73), so that the physical thickness of the shock is independent of N . We used the second series to test the convergence of our scheme.

Figures 11 to 14 give the calculation result for $N = 1000$ and $t = 0.1$, for tests 1 and 2 and first- and third- order schemes. We can see that all four results are good in capturing shocks. The shock is broader for test 1 than for test 2, since the coefficient for the artificial viscosity is larger for test 1. On the other hand, weak oscillation is visible in the left-hand-side region of the contact discontinuity, in particular for the third-order scheme.

In test 1, we compare results with $N = 1000, 2000, 4000, 8000$ to the analytical solution. Since it is difficult to derive the analytical solution for test 2, we compare the results with $N = 1000, 2000, 4000, 8000, 16000$ to that with $N = 32000$. We calculate the errors of the total energy and the total momentum in the region $-0.25 \leq x \leq 0.25$ as the measure of the conservative quantities. These errors are given by

$$\epsilon_{\text{ene}} = \frac{|E - E_a|}{|E_{0.1}|}, \quad (74)$$

$$\epsilon_{\text{mom}} = \frac{|p - p_a|}{|p_{0.1}|}, \quad (75)$$

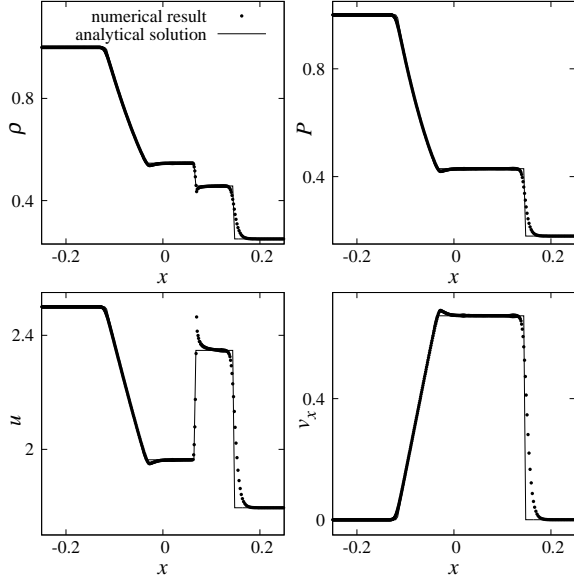


Fig. 11. Result of test 1 at $t = 0.1$ with first-order CPHSF.

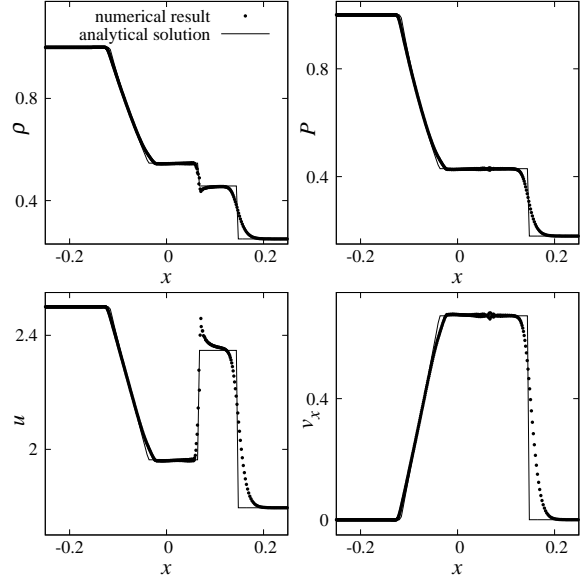


Fig. 12. Same as figure 11, but the results with third-order CPHSF.

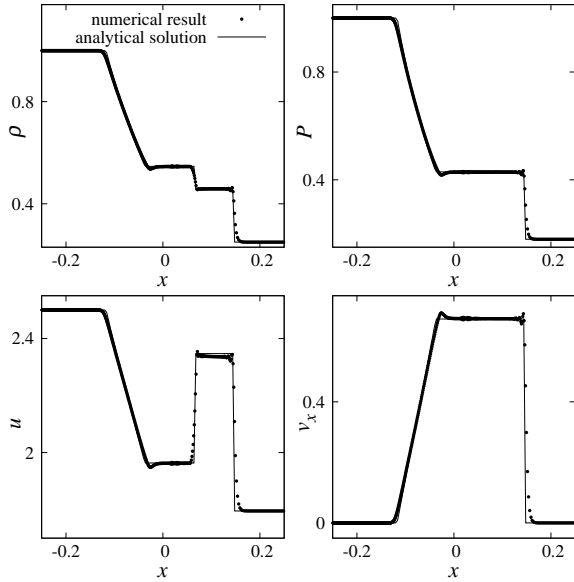


Fig. 13. Result of test 2 at $t = 0.1$ with first-order CPHSF.

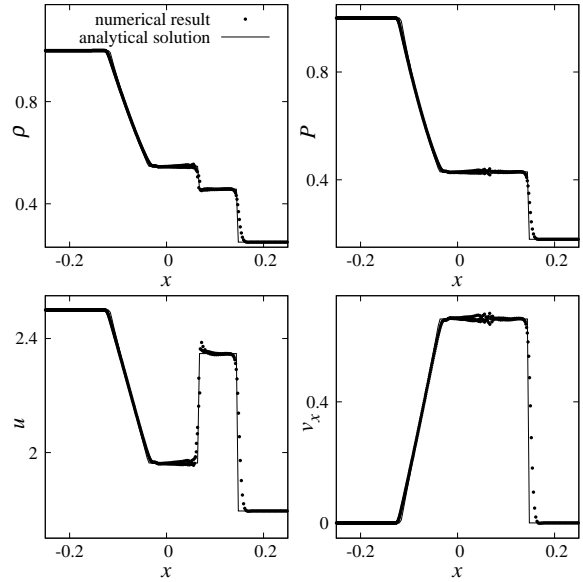


Fig. 14. Same as figure 13, but the results with third-order CPHSF.

where E and p are numerical solutions of energy and the momentum, and E_a and p_a are analytical solutions of energy and the momentum (test 1) or the results of $N = 32000$ calculation (test 2). The parameters $E_{0.1}$ and $p_{0.1}$ are the values of E_a and p_a at $t = 0.1$. Energy and the momentum of the numerical solution are calculated by

$$E = \int_{-0.25}^{0.25} \hat{u} + \frac{1}{2} \hat{\rho} \hat{v}_x^2 dx, \quad (76)$$

$$p = \int_{-0.25}^{0.25} \hat{\rho} \hat{v}_x dx, \quad (77)$$

where \hat{u} , $\hat{\rho}$ and \hat{v}_x are internal energy, density and velocity of the numerical solution. Using the shape functions, this integral is expressed as

$$E \simeq \sum_m^n \sum_{i, |x_i| \leq 0.25} \frac{[(x_{i+1} - x_i)^{m+1} - (x_i - x_{i-1})^{m+1}]}{2^{m+1}(m+1)} \sum_j \left(u_j + \frac{\rho_j}{2} v_{x,j}^2 \right) \Psi_{m,ij}, \quad (78)$$

$$p \simeq \sum_m^n \sum_{i, |x_i| \leq 0.25} \frac{[(x_{i+1} - x_i)^{m+1} - (x_i - x_{i-1})^{m+1}]}{2^{m+1}(m+1)} \sum_j \rho_j v_{x,j} \Psi_{m,ij}, \quad (79)$$

where n is the spatial order of the scheme. The parameter $\Psi_{m,ij}$ is the m -th differential-order shape function.

Figure 15 shows the time evolutions of ϵ_{ene} and ϵ_{mom} with first- and third-order schemes and $N = 1000, 2000, 4000, 8000$ for test 1. We can see that the error is proportional to $1/N$. In test 1, the initial smoothing length x_0 and the strength of the artificial viscosity depend on $1/N$ in a linear way, and thus the errors of the fluid equation and artificial viscosity are of zeroth order. The width of region, where these error occurs, is proportional to $1/N$. Therefore, the total errors at the shock become $\mathcal{O}(1/N)$.

Figure 16 show the time evolutions of ϵ_{ene} and ϵ_{mom} with first- and third-order schemes and $N = 1000, 2000, 4000, 8000, 16000$ for test 2. We can see that the error is much smaller than those in figure 15. If the result converge to an exact solution following the order of the scheme, the error relation to $N = 32000$ result should be given by $\epsilon \propto 1/N^{n+1} - 1/(32000)^{n+1}$ where n is the order of the scheme.

In figure 17, we plot the error at $t = 0.1$ as a function of N . We can see that the result of test 2 with third-order scheme actually shows the $\mathcal{O}(N^{-4})$ error, demonstrating that the spatial order of our CPHSF scheme is consistent with the numerical order with of the fitting polynomial.

3.3 Rotating cone test

In this section, we present the result of the rotating cone test (e.g. Crowley 1968, Chock 1991, Vijay 1998) to discuss the effect of the numerical diffusion caused by the rearrangement. In this test, the rigid rotation a cone-shaped object is followed for two complete circles. Since CPHSF is fully Lagrangian scheme, without the rearrangement of particles it will perfectly conserve the initial shape of the object. We forced the periodic rearrangement of particles to see its effect.

We used the initial condition the same as in Vijay (1998). The computational domain is $-32 \leq x \leq 32, -32 \leq y \leq 32$. The initial density distribution is given by

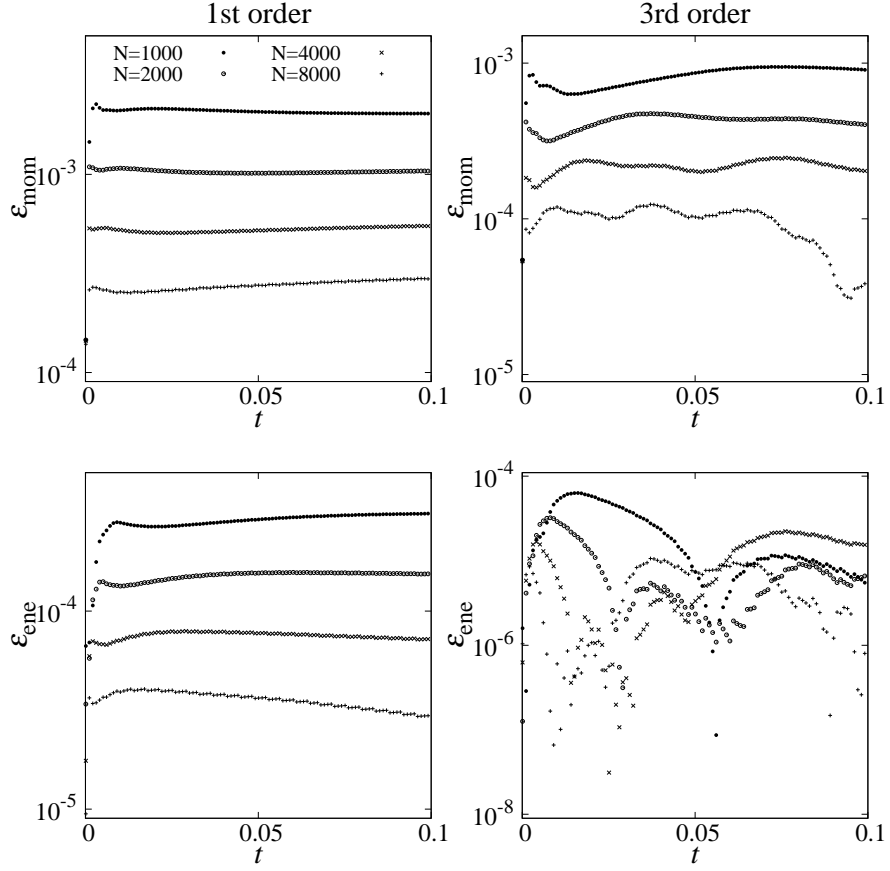


Fig. 15. The upper panels show ϵ_{mom} and the lower panels show ϵ_{ene} . The left-hand side is the result of first-order CPHSF and the right is that of third-order one.

$$\rho(r_c) = \begin{cases} \frac{\rho_{\text{back}} - \rho_{\text{peak}}}{\Delta r} r_c + \rho_{\text{peak}} & r_c < \Delta r \\ \rho_{\text{back}} & \text{otherwise} \end{cases} \quad (80)$$

$$r_c = \sqrt{(x - 16)^2 + y^2}, \quad (81)$$

where $\rho_{\text{peak}} = 100$, $\rho_{\text{back}} = 5$ and $\Delta r = 32/(\sqrt{N} - 1)$ where N is the number of particles. Initial velocity is the rigid body rotation given by

$$v_x = -\omega_{\text{cone}} y, \quad (82)$$

$$v_y = \omega_{\text{cone}} x, \quad (83)$$

where ω_{cone} is the angular velocity and we set $\omega_{\text{cone}} = 0.28$. We integrate position and velocity with respect to time analytically. The time step is given by

$$\Delta t = \frac{\pi}{32\omega} \quad (84)$$

In this test, we use first-, third- and fourth-order schemes. The numbers of particles are $N =$

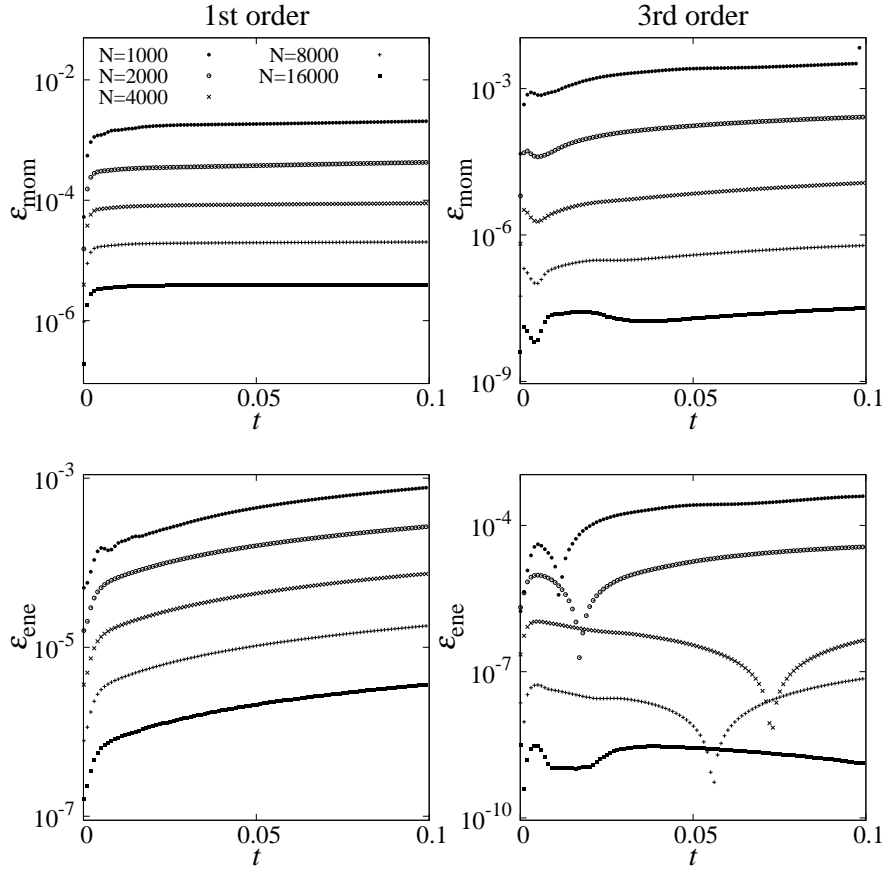


Fig. 16. Same as figure 15, but for test 2.

33×33 and 129×129 . We rearrange particles to the grid pattern n_{rea} times within two rotations. We compare the results with $n_{\text{rea}} = 8, 4, 2, 1$ and 0. We rearrange at $(16m + 8)$ -th, $(32m + 8)$ -th, $(64m + 24)$ -th and 72-th steps when the rotating angle is $\pi/4 + m\pi/2$ ($m \in \mathbb{N}$) for $n_{\text{rea}} = 8, 4, 2$ and 1.

Figures 18-21 show cones after two rotations for the number of particles $N = 33 \times 33$ and $N = 129 \times 129$. The orders of schemes are first and fourth.

Table 1 shows the errors of the height of the cone after two rotations defined as

$$\left| 1 - \frac{\rho(x=16, y=0)}{\rho_{\text{peak}}} \right|, \quad (85)$$

We derive $\rho(x=16, y=0)$ using equation (9) when n_{rea} is not zero since, due to the rearrangement, there is no particle at $(x, y) = (16, 0)$. We can see that the errors are smaller for larger n_{rea} , higher order schemes, and higher resolution (larger number of particles). The error for the case of $N = 129 \times 129$ and the fourth-order scheme are better or similar to those of mesh and mesh-free schemes discussed in Chock (1991) or Vijay (1998), except for those of extremely high accuracy schemes based on Fourier

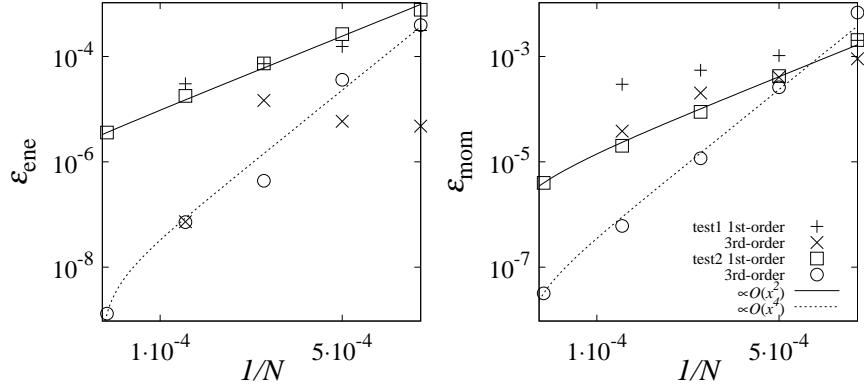


Fig. 17. The errors ϵ_{ene} (left) and ϵ_{mom} (right) at $t = 0.1$ plotted against $1/N$. Crosses and “X”s show the results with first- and third-order CPSHSF for test 1, and squares and circles those for test 2. Solid and dashed curves show the theoretical models for the error of first- and third-order schemes for test 2.

transform and one of finite-volume scheme which the interpolynomial is a cubic spline (Yamartino 1993). In our initial model, we used only one particle to express the peak, while in the traditional rotating cone test, four grid points are used to express the peak. Thus, with our initial condition it is much harder to keep the height of the peak. Thus, we can conclude that even when we forced frequent rearrangement of particles, our scheme can achieve the accuracy comparable to those of high-order Eulerian schemes. Note that the required frequency of the rearrangement is generally quite low. For example, the total number of rearrangement in the Kelvin-Helmholtz instability test with the first-order scheme discussed in section 3.4.1 is 9 in 5291 timesteps.

Table 1. The errors of density peaks.

		$n_{\text{rea}} = 8$	$n_{\text{rea}} = 4$	$n_{\text{rea}} = 2$	$n_{\text{rea}} = 1$	$n_{\text{rea}} = 0$
$N = 33 \times 33$	1st	6.53×10^{-1}	5.19×10^{-1}	4.05×10^{-1}	3.29×10^{-1}	0.00
	3rd	5.32×10^{-1}	4.29×10^{-1}	3.43×10^{-1}	2.86×10^{-1}	0.00
	4th	4.07×10^{-1}	3.27×10^{-1}	2.63×10^{-1}	1.89×10^{-1}	0.00
$N = 129 \times 129$	1st	1.79×10^{-1}	1.33×10^{-1}	1.02×10^{-1}	8.26×10^{-2}	0.00
	3rd	1.01×10^{-1}	8.49×10^{-2}	7.30×10^{-2}	6.46×10^{-2}	0.00
	4th	7.76×10^{-2}	6.85×10^{-2}	6.11×10^{-2}	5.56×10^{-2}	0.00

3.4 Kelvin-Helmholtz Instability test

The Kelvin-Helmholtz instability (hereafter KHI) test has been used to investigate the ability of numerical schemes to handle large deformations and hydrodynamical instabilities (Okamoto et al. 2003, Agertz et al. 2007, Price 2008, McNally et al. 2012). We performed two-dimensional KHI from two different initial conditions. One is used in Price (2008), and another is in McNally et al. (2012). The

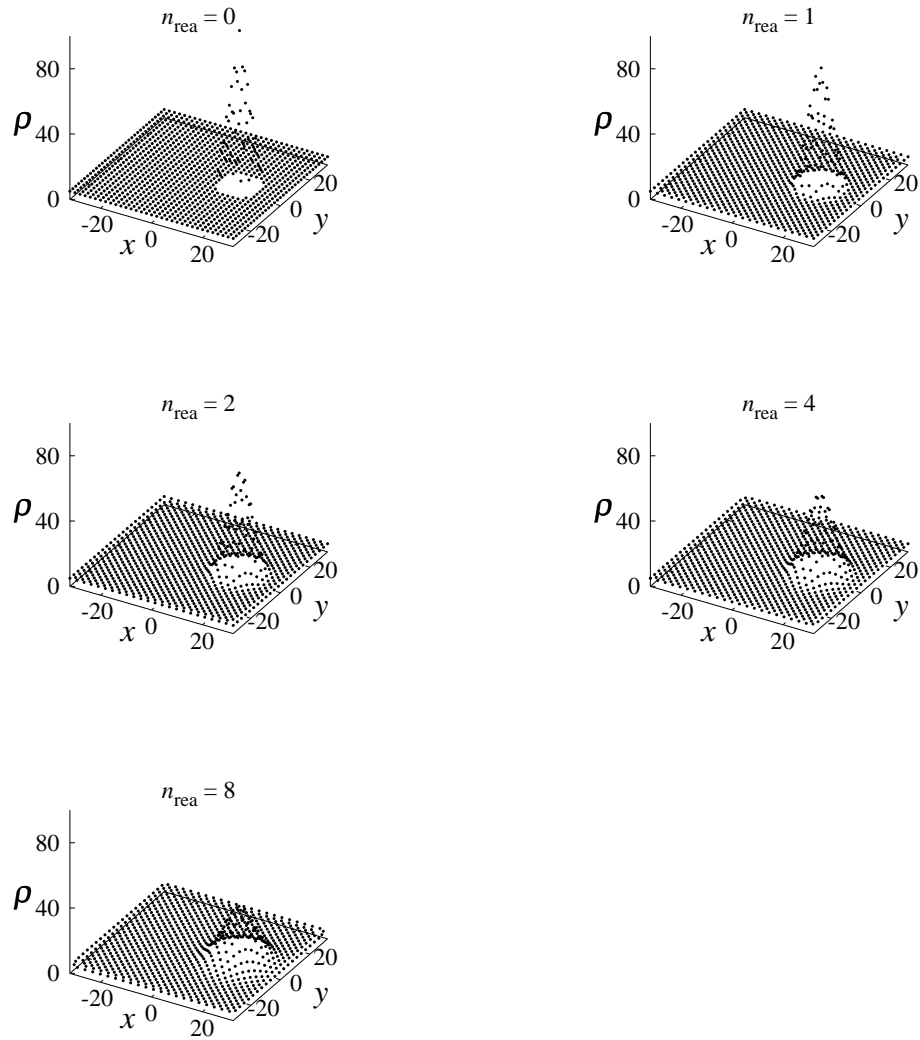


Fig. 18. Results of the rotating cone test with $N = 33 \times 33$ and the first-order scheme. From left top to right bottom, the result without the rearrangement and with $n_{\text{rea}} = 128, 64, 32, 16$ and 8 .

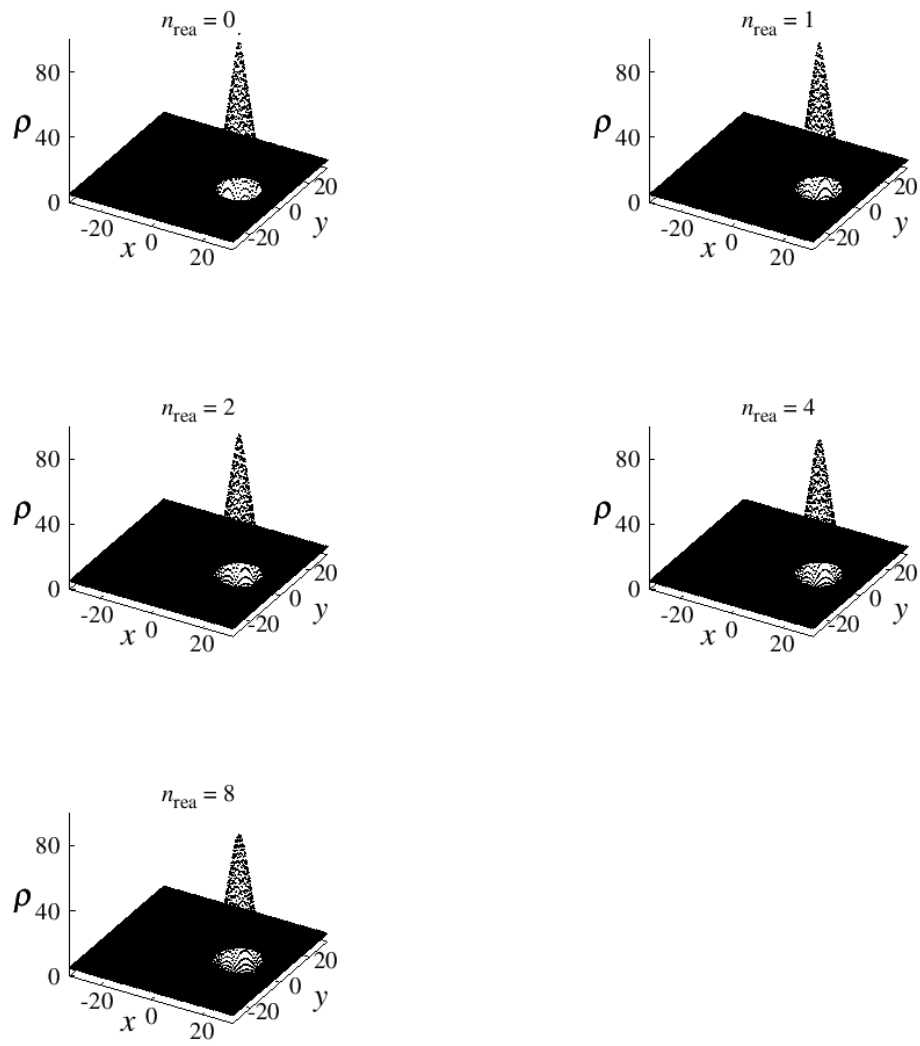


Fig. 19. The same as figure 18, but for $N = 129 \times 129$.

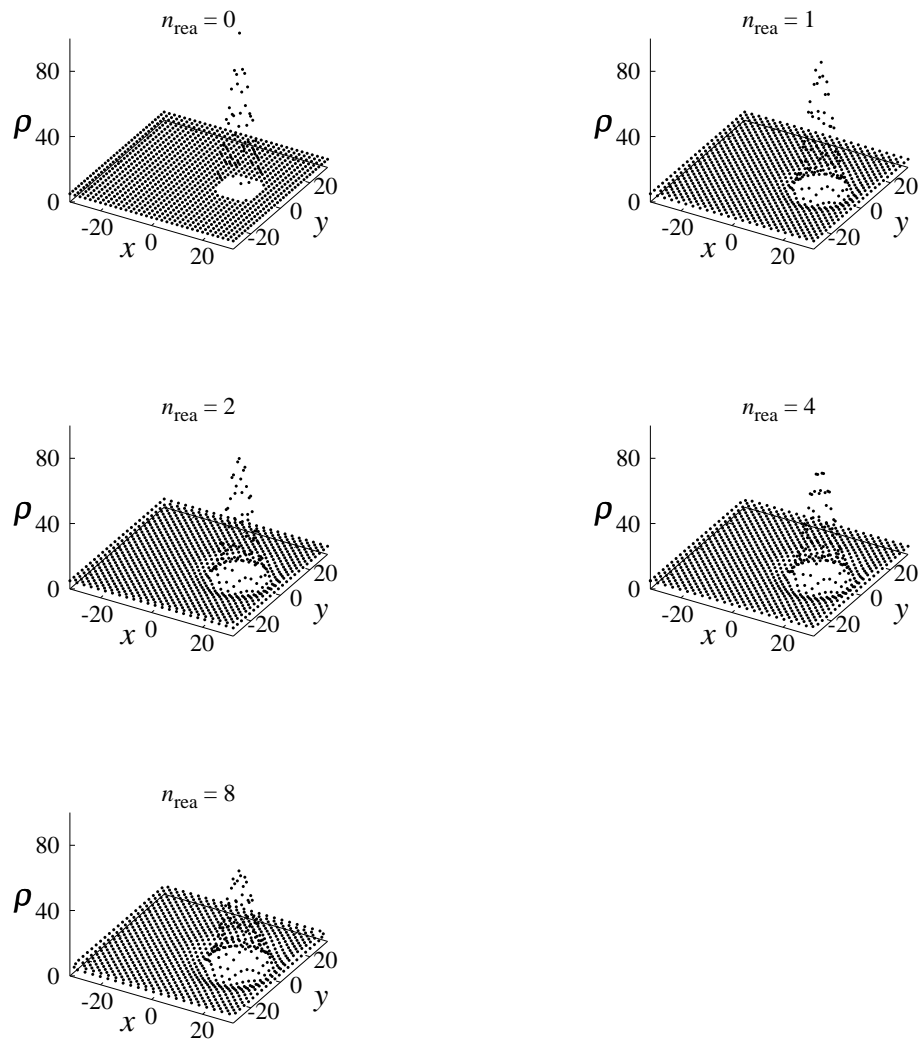


Fig. 20. The same as figure 18, but for the fourth-order scheme.

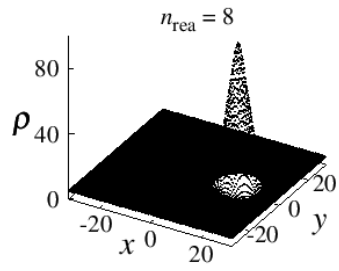
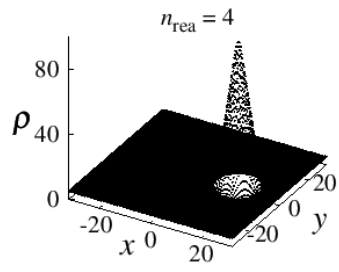
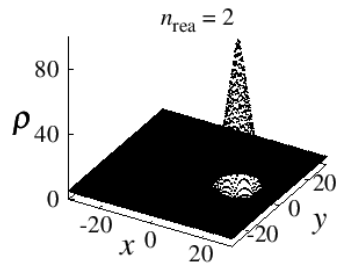
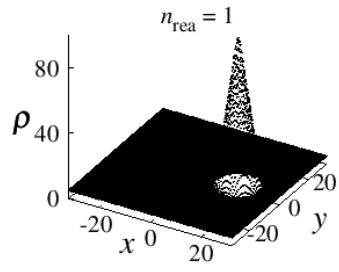
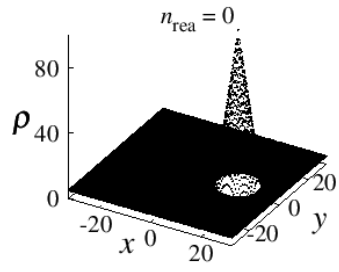


Fig. 21. The same as figure 20, but for $N = 129 \times 129$.

difference between two initial conditions is that density and shear velocity are discontinuous in Price (2008), while smoothed in McNally et al. (2012). We present the results of calculations with the initial condition in McNally et al. (2012) in section 3.4.1 and that in Price (2008) in section 3.4.2.

3.4.1 Kelvin-Helmholtz Instability test with smoothed initial density

We performed two-dimensional calculations using a computational domain of $0 \leq x < 1, 0 \leq y < 1$, with a periodic boundary condition. We made the smoothed contact discontinuity by setting the initial conditions as

$$\rho(y) = \begin{cases} \rho_l - \rho_m e^{(y-0.25)/\Delta y}, & 0 \leq y < 0.25 \\ \rho_h + \rho_m e^{(0.25-y)/\Delta y}, & 0.25 \leq y < 0.5 \\ \rho_h + \rho_m e^{(y-0.75)/\Delta y}, & 0.5 \leq y < 0.75 \\ \rho_l - \rho_m e^{(0.75-y)/\Delta y}, & 0.75 \leq y < 1 \end{cases} \quad (86)$$

where we used $\Delta y = 0.025$, $\rho_h = 2$ and $\rho_l = 1$. The parameter ρ_m is given by $\rho_m = (\rho_l - \rho_h)/2$. The smoothed velocity of the x -direction (shear velocity) is

$$v_x(y) = \begin{cases} v_l - v_m e^{(y-0.25)/\Delta y}, & 0 \leq y < 0.25 \\ v_h + v_m e^{(0.25-y)/\Delta y}, & 0.25 \leq y < 0.5 \\ v_h + v_m e^{(y-0.75)/\Delta y}, & 0.5 \leq y < 0.75 \\ v_l - v_m e^{(0.75-y)/\Delta y}, & 0.75 \leq y < 1 \end{cases} \quad (87)$$

where v_h and v_l are the reference values of the x -directional velocity in the high- and low-density regions, respectively. We used $v_h = -0.5$ and $v_l = 0.5$. We assume that fluid is an ideal gas with $\gamma = 5/3$ and set $P = 2.5$ and $v_y = 0$. The number of particles is 256×256 . The velocity perturbation in the y -direction is as follows:

$$\Delta v_y(x) = A \sin[2\pi x/\lambda], \quad (88)$$

where $\lambda = 0.5$ and $A = 0.01$. The growth timescale of KHI is

$$\tau_{\text{KH}} = \frac{\lambda(\rho_h + \rho_l)}{\sqrt{\rho_h \rho_l} |v_h - v_l|}. \quad (89)$$

For our setup, $\tau_{\text{KH}} = 1.06$.

We rearranged particles with $c_{\text{rea}} = 0.55$ for the first-order CPHSF and $c_{\text{rea}} = 0.5$ for the third-order one.

Figures 22 and 23 show the results obtained using first- and third-order schemes. The first-order result looks similar to the highest resolution Pencil Code result of McNally et al. (2012). In figure 23, we can clearly see the development of the second-level KHI, which does not exist in the first-order result. Thus, we can conclude that the effective resolution of the third-order scheme is significantly higher than that of the first-order scheme with the same number of particles.

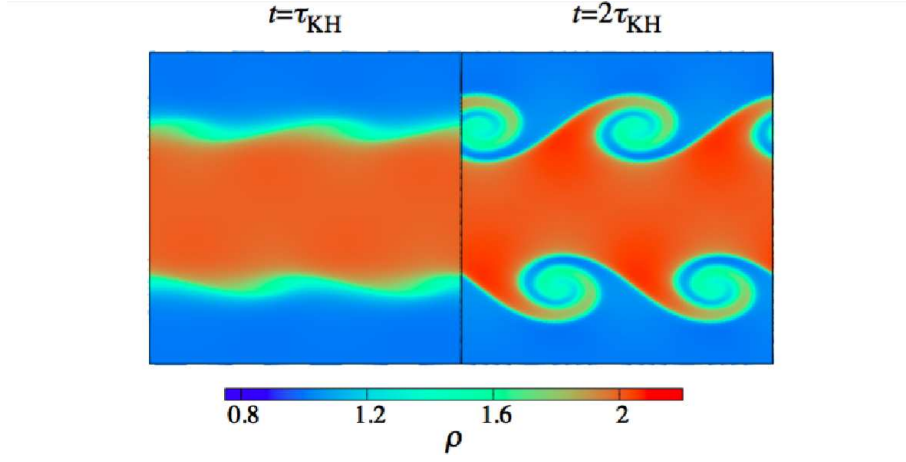


Fig. 22. Result of the KHI test with smoothed initial density. Density distributions at $t = \tau_{kh}, 2\tau_{kh}$ from left to right. The order of the scheme is first.

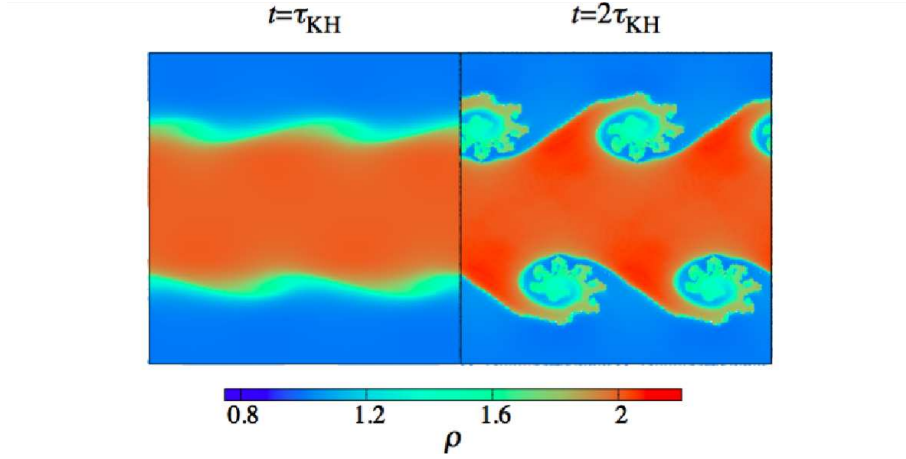


Fig. 23. The same as figure 22, but for the third-order scheme.

3.4.2 Kelvin-Helmholtz Instability test with sharp initial density

The initial condition is same as that in section 3.4.1, except for density, shear velocity and the perturbation. In this simulation, initial density is given by

$$\rho(y) = \begin{cases} \rho_l, & 0 \leq y < 0.25, 0.75 \leq y < 1 \\ \rho_h, & 0.25 \leq y < 0.75 \end{cases} \quad (90)$$

where we used $\rho_h = 1$ and $\rho_l = 2$. Velocity of the x -direction is

$$v_x(y) = \begin{cases} v_l, & 0 \leq y < 0.25, 0.75 \leq y < 1 \\ v_h, & 0.25 \leq y < 0.75 \end{cases} \quad (91)$$

where we used $v_h = -0.5$ and $v_l = 0.5$. The velocity perturbation in the y -direction is

$$\Delta v_y(x) = \begin{cases} A \sin[-2\pi(x + 0.5)/\lambda], & 0 \leq |y - 0.25| \leq 0.025 \\ A \sin[2\pi(x + 0.5)/\lambda], & 0 \leq |y - 0.75| \leq 0.025 \end{cases} \quad (92)$$

where $\lambda = 1/6$ and $A = 0.025$. For our setup, $\tau_{\text{KH}} = 0.35$.

We rearranged particles with $c_{\text{rea}} = 0.55$ for the first-order CPHSF and $c_{\text{rea}} = 0.4$ for the third-order one.

Figures 24 and 25 show the results obtained using first- and third-order schemes. The vortexes in our result are clearer than that of Price (2008) in which SPH with the artificial conductivity is used. We conclude that CPHSF can handle KHI, even if the initial density and shear velocity at the contact discontinuity are really discontinuous.

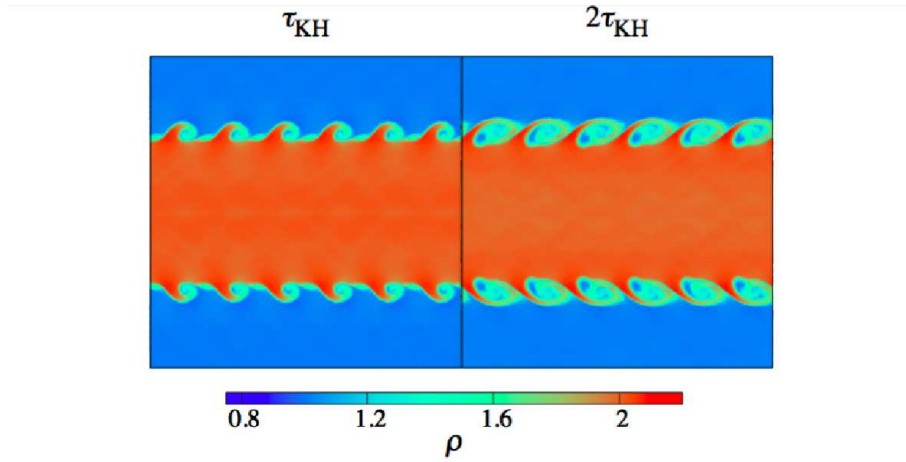


Fig. 24. Result of the KHI test with sharp initial density. Density distributions at $t = \tau_{\text{kh}}, 2\tau_{\text{kh}}$ from left to right. The order of the scheme is first.

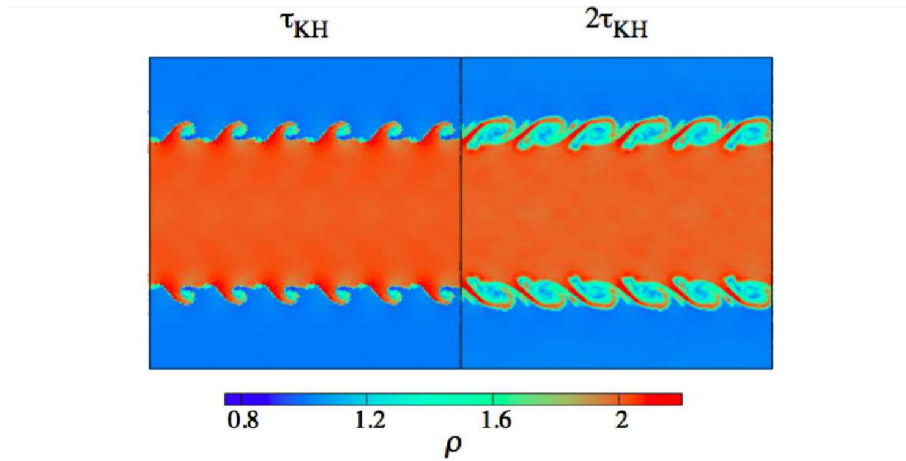


Fig. 25. The same as figure 24, but for the third-order scheme.

3.5 Rayleigh-Taylor Instability test

The Rayleigh-Taylor instability (hereafter RTI) test is one of popular tests to investigate the capability of the scheme to handle fluid instability. We used the initial condition the same as in Saitoh & Makino (2013). The computational domain is $0 \leq x \leq 1$, $0 \leq y \leq 1$, and the boundary of two fluids is at $y = 0.5$. We applied a periodic boundary condition at $x = 0, 1$ and equation (56) at $y = 0, 1$ as boundary conditions. The number of particles is 256×257 . The gravitational acceleration is -0.5 . Initial velocity is $v_x = 0$ and $v_y = 0$. Initial density is

$$\rho(y) = \begin{cases} \rho_l \left[1 + \frac{\gamma-1}{\gamma} \frac{\rho_l g(y-0.5)}{P_0} \right], & 0 \leq y \leq 0.5 \\ \rho_h \left[1 + \frac{\gamma-1}{\gamma} \frac{\rho_h g(y-0.5)}{P_0} \right], & 0.5 \leq y \leq 1 \end{cases} \quad (93)$$

where we used $\rho_h = 2$ and $\rho_l = 1$. Since the fluid is in equilibrium, initial pressure is given by

$$P(y) = \begin{cases} P_0 \left(\frac{\rho}{\rho_l} \right)^\gamma, & 0 \leq y \leq 0.5 \\ P_0 \left(\frac{\rho}{\rho_h} \right)^\gamma. & 0.5 \leq y \leq 1 \end{cases} \quad (94)$$

where P_0 is the pressure at the boundary of two fluids, and we used $P_0 = 10/7$ in this test. The velocity perturbation in the y -direction for $0.3 \leq y \leq 0.7$ is

$$\Delta v_y(x, y) = \delta_{vy} [1 + \cos(4\pi x)] \{1 + \cos[5\pi(y - 0.5)]\}, \quad (95)$$

where we used $\delta_{vy} = 0.025$.

We used equation (41) with $c_{rea} = 0.55$ for the rearrangement of particles. Since equation (41) cannot be applied to particles near the surface, we excluded particles with $y < 0.05$ or $y > 0.95$ when evaluating equation (41).

Figure 26 shows the result. We can see that CPHSF can handle RTI. We can see small-scale KHI features develop near the bottom of the heavier fluid, and we can also see small-scale RTI features near the ‘‘root’’ of sinking heavier fluid. These fine features indicate that CPHSF has high resolution and small dissipation.

3.6 Gravity wave test

The gravity wave test is useful to investigate the capability of numerical schemes to handle the free surface. Note that standard SPH cannot handle the gravity wave well, because it cannot correctly evaluate the density of particles near the surface. SPH schemes specially designed to handle free surface exist (e.g. Monaghan 1994, Antuono et al. 2011). However, the most sophisticated schemes require local high-order diffusion of velocity to stabilize the wave (e.g. Antuono et al. 2011). The computational domain is $0 \leq x < 1$, $0 \leq y < 1$. We applied a periodic boundary at $x = 0$, equation (55) at $y = 0$ and equation (56) for particles initially at $y = 1$ as boundary conditions. The number of

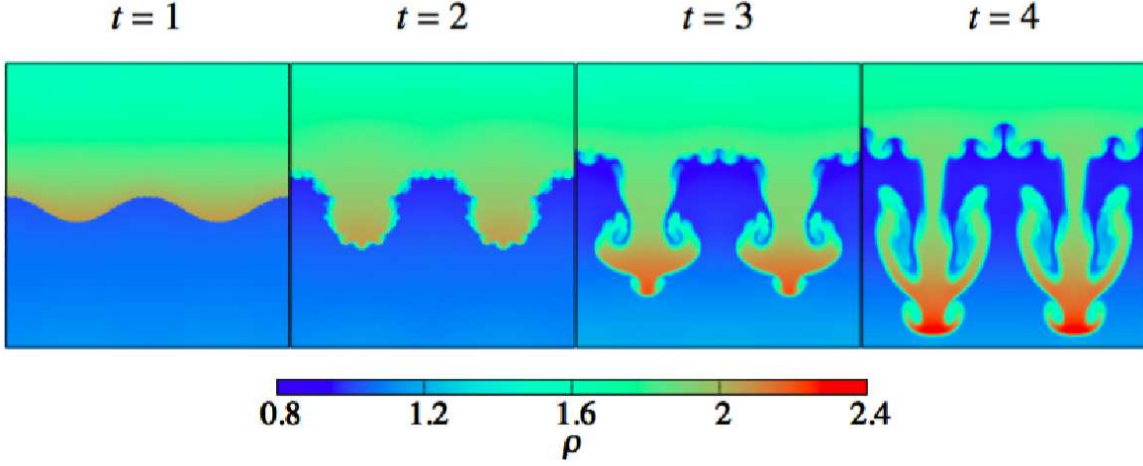


Fig. 26. Result of the RTI test with sharp initial density. Density distributions at $t = 1, 2, 3$ and 4 from left to right. The order of the scheme is first.

particles is 50×51 . The equation of state is given by equation (49) with $g = -10$, $\rho_{\text{air}} = 1000$ and $P_{\text{air}} = 10^5$, and initial density is

$$\rho(y) = \rho_{\text{air}} e^{g(H-y)/c_{s0}^2}. \quad (96)$$

Initial velocity is the same as in Antuono et al. (2011),

$$v_x = A \frac{|g|k}{\omega} \frac{\cosh(ky)}{\cosh(kH)} \sin(kx), \quad (97)$$

$$v_y = -A \frac{|g|k}{\omega} \frac{\sinh(ky)}{\cosh(kH)} \cos(kx), \quad (98)$$

where A , k and ω are the amplitude, the number of wave and the frequency. In this test, we set $A = 0.01$, $k = 2\pi/L$ and $\omega = \sqrt{|g|k \tanh(kH)}$. We used $\zeta_{\min} = 0.1$.

Figure 27 shows the time evolution up to $t = 0.75T$. Figure 28 and figure 29 show the error of velocity at $(x, y) = (0.25, 1)$ for runs with the number of particles N , 50×51 , 100×101 and 151×150 . The error is given by

$$\epsilon_{v_x} = |v_x - v_{x,0}|, \quad (99)$$

$$\epsilon_{v_y} = |v_y - v_{y,0}|, \quad (100)$$

where $v_{x,0}$ and $v_{y,0}$ are analytical solutions. We can see that the error becomes smaller as we increase N , showing the first-order convergence, as we used the first-order scheme.

Figure 30 shows y of the particle initially at $(x, y) = (0, 1)$. In an initial stage, the phases of results for $N = 2550$, 10100 and 22650 agree well with each other. However, the wave for $N = 2550$ has slightly longer period than those of $N = 10100$ and $N = 22650$, and the difference of y between the result of $N = 2550$ and those of $N = 10100$ and $N = 22650$ grows in time. In addition, the phase

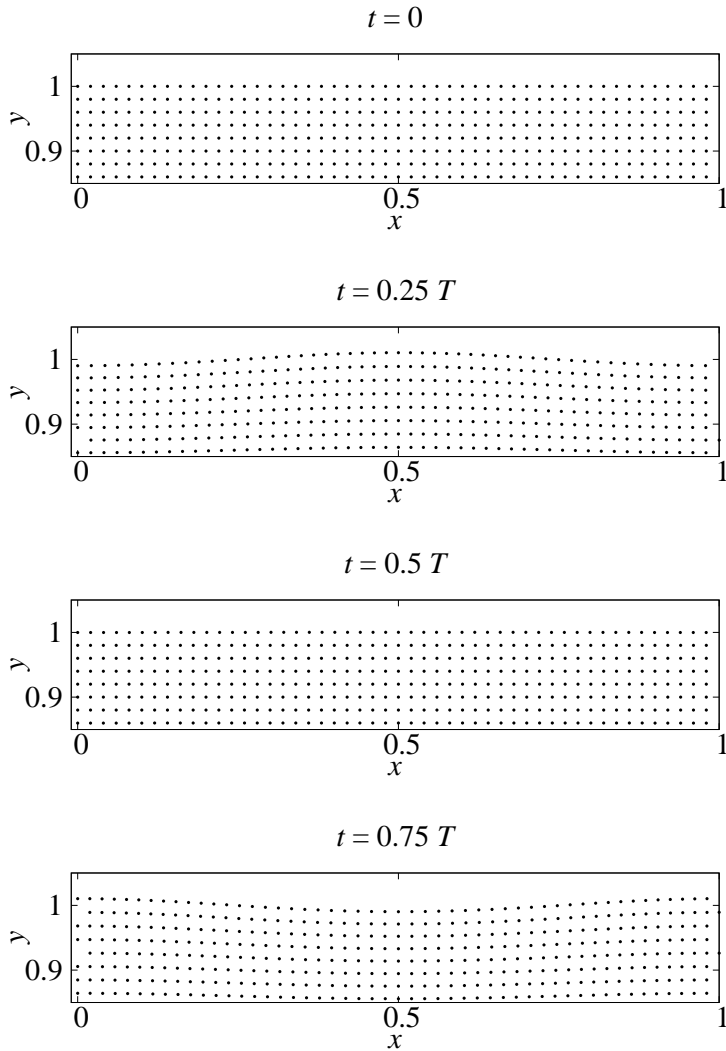


Fig. 27. Results of gravity wave test, from top to bottom, the snapshots at $t = 0$, $0.25T$, $0.5T$ and $0.75T$ are shown.

of $N = 10100$ deviates from that of $N = 22650$ slightly at the later stage.

3.7 Dam break test

The dam break test is the most widely used test for numerical schemes for the fluid with the free surface. The initial condition of the dam break test is the same as that used by Monaghan (1994). The computational domain is $0 \leq x \leq 0.6$, $0 \leq y \leq 0.6$. We applied equation (55) at $x = 0.6$ and $y = 0.6$ and equation (56) at $x = 0$ and $y = 0$ as boundary conditions. The number of particles is 60×61 . We

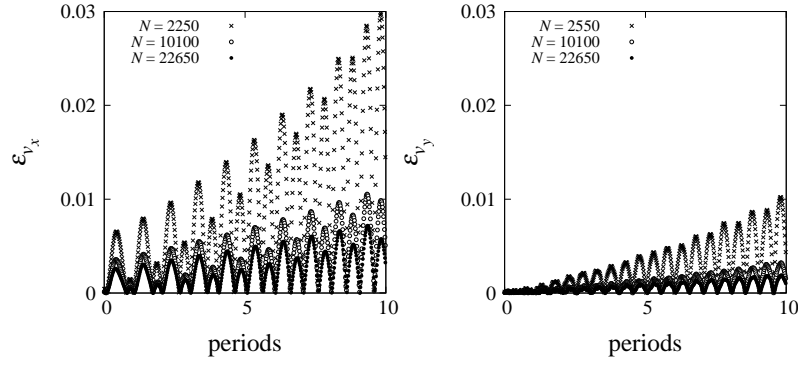


Fig. 28. The errors of x - and y -directional velocity at $(x, y) = (0.25, 1)$ in the gravity wave test with the numbers of particles N 2550, 10100, 22650.

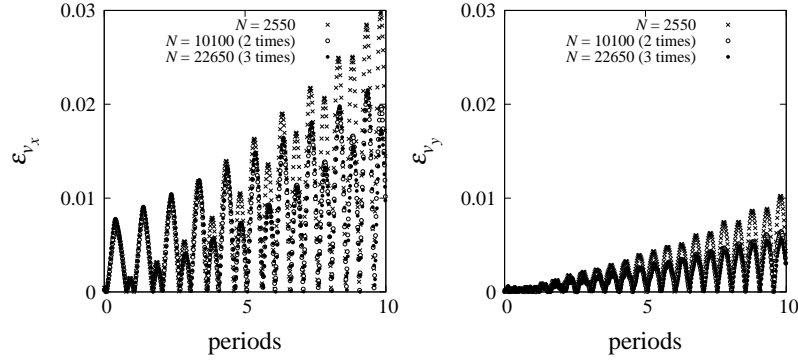


Fig. 29. The same as figure 28, but the error with $N = 10100$ is multiplied by two, while that with $N = 22650$ is multiplied by three.

set that the equation of state is given by equation (49) with $g = -9.8$, $\rho_{\text{air}} = 1000$ and $P_{\text{air}} = 10^5$, and initial density is

$$\rho(y) = \rho_{\text{air}} \left[\frac{6|g|}{7C_B} \rho_{\text{air}} (0.6 - y) + 1 \right]^{1/6}. \quad (101)$$

We set that density and pressure of the particles at $x = 0.6$ is

$$\rho = \rho_{\text{air}}, \quad (102)$$

$$P = P_{\text{air}}, \quad (103)$$

Initial velocity is $v_x = v_y = 0$.

In dam break simulation, the rearrangement of particles is necessary. We rearrange particles every 0.01 time unit. We used $C_{\text{CFL}} = 0.05$.

Figure 31 shows the time evolution up to $t = 0.7$. The result looks similar to those in the previous dam break test (Monaghan 1994). Figure 32 gives the position of the forefront of water

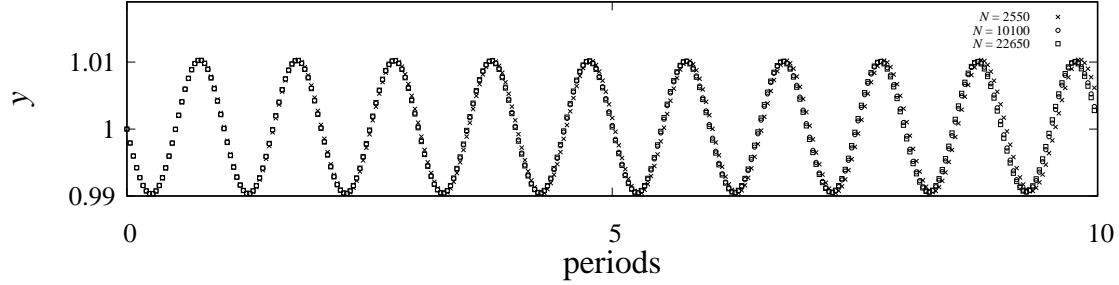


Fig. 30. Time evolution of the y -coordinate of the particle initially at $(x, y) = (0, 1)$ in the gravity wave test in which the numbers of particles N are 2550, 10100, 22650.

plotted against t^* , where t^* is the dimensionless time defined as $t^* = t\sqrt{|g|/H}$. The results are for first-order CPHSF, an analytical solution (Whitham 1999) and the experimental data of Martin & Moyce (1952), by Lobovský et al. (2014) distributed ¹. It was compared to numerical solutions in previous studies (e.g. Monaghan 1994, Staroszczyk 2010). According to Whitham (1999), the forefront velocity v_{dw} becomes $v_{\text{dw}} = 2\sqrt{|g|H}$ in static state, if we use on the theory of shallow water waves. Therefore, the position of the forefront is $2\sqrt{|g|H}t$ analytically.

Note that the analytical solution is not exact. Clearly, in the limit of $t^* \rightarrow 0$, the solution should be quadratic and not linear in time. The experimental result is not free from the real viscosity. Therefore, the discrepancy between our numerical result and experimental result does not imply the problem in the side of our scheme. Staroszczyk (2010) calculated the dam break using his CSPH and standard SPH schemes and compared the result with the experimental data. The agreement between numerical and experimental data was actually pretty good, better than that in our case. This result probably imply both of experimental result and Staroszczyk (2010)'s result suffer the effect of viscosity on other dispational effect. Though Staroszczyk (2010) did not explicitly use AV, he applied the re-evaluation of the density, which would cause significant dissipation. Therefore, we believe our scheme is less dissipative than his CSPH.

3.8 Cold Keplerian disk test

The cold Keplerian disk is important in astronomy. We prepared a two-dimensional computational domain of $0.5 \leq r < 2$. We applied equation (55) at the inner edge and equation (56) at the outer edge as boundary conditions. The number of particles is 46368, and we place the particles in concentric rings with the same intervals for r axis and θ axis. We assumed that the fluid is ideal gas with $\gamma = 1.4$

¹ <http://canal.etsin.upm.es/papers/lobovskyyetaljfs2014/>

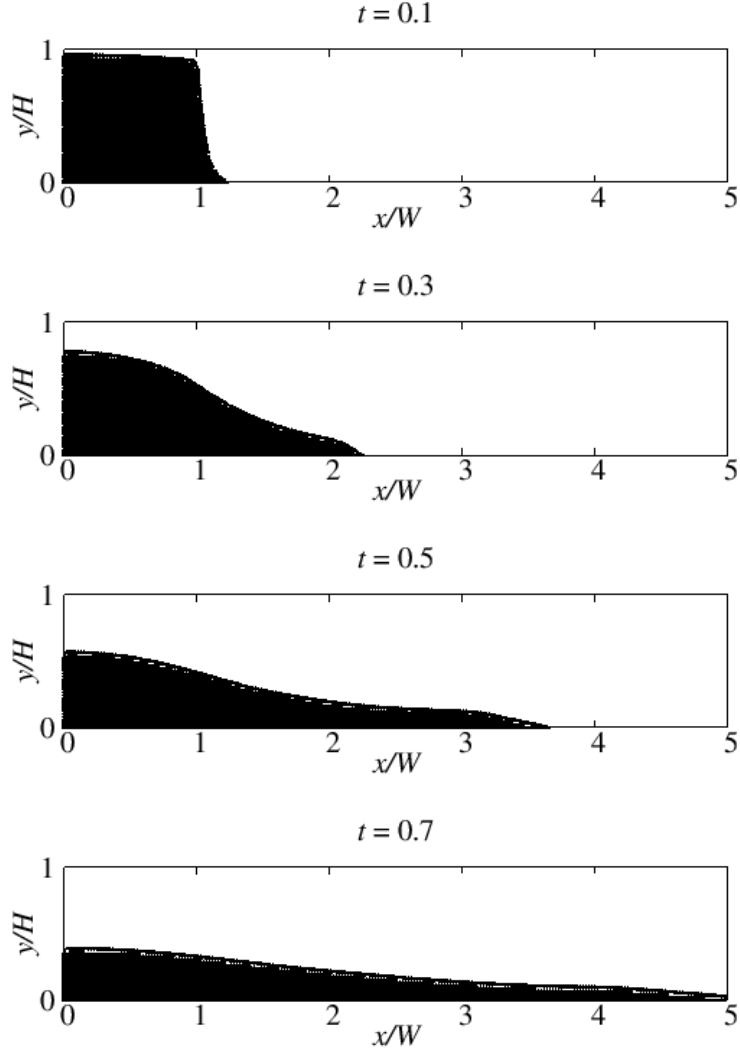


Fig. 31. Result of the dam break test. The snapshots at $t = 0, 0.25T, 0.5T$ and $0.75T$ from top to bottom.

and set $\rho = 1$ and $P = 10^{-6}$. Initial velocity is the pure Keplerian rotation given by

$$v_x = -\sqrt{\frac{GM_*}{r}} \frac{y}{r}, \quad (104)$$

$$v_y = \sqrt{\frac{GM_*}{r}} \frac{x}{r}, \quad (105)$$

where G is the gravitational constant and M_* is the mass of the central star. We set $GM_* = 1$. The time step is smaller one between the time step given by the Courant conditions for the pressure gradient term and the central force term. Therefore, we compare equation (52) with

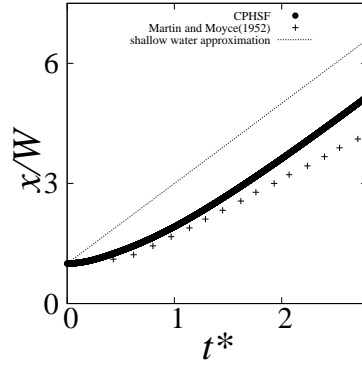


Fig. 32. The forefront of water in the dam break test plotted against t^* . Filled circles, crosses show the result of first-order CPHSF and experimental result (see text), respectively. The solid line indicate the analytic estimate based on the shallow water equation.

$$\Delta t = \min_i c_{\text{disk}} \sqrt{\frac{r_i}{\|\mathbf{a}_i\|}}, \quad (106)$$

and then smaller one is taken. The parameter c_{disk} is a constant coefficient, and the value of $2\pi/c_{\text{disk}}$ denotes how many steps is calculated in a orbit. We set $2\pi/c_{\text{disk}} = 50$.

In this test, we used fourth-order CPHSF, because the accuracy of the approximation of the artificial viscosity is important to prevent unphysical angular momentum transfer (e.g. Cullen & Dehnen 2010). In addition, we use fifth-order Radau method for the time integration.

Figure 33 shows the results. We can see that the disk does not break till $t \simeq 2000$ orbits. Note that this lifetime is longer than the lifetime of any Lagrangian scheme, reported in the literature (Hopkins 2015, Hosono et al. 2016) by more than a factor three.

Figure 34 shows the error of the density plotted against time. The error is given by

$$\epsilon_{\text{dens}} = \max_i |\rho_i - 1|. \quad (107)$$

It is clear that the error grows rapidly after $t = 1400$ orbits. From figure 33, we can see that the error becomes large at the outer edge after $t = 1500$ orbits. Therefore, if we can improve the treatment of the outer edge, we may be able to reduce the error. We conclude that the cold Keplerian disk integrated using CPHSF can survive for > 1000 orbits. CPHSF can handle rotating disks better than the Lagrangian scheme variants proposed in previous studies.

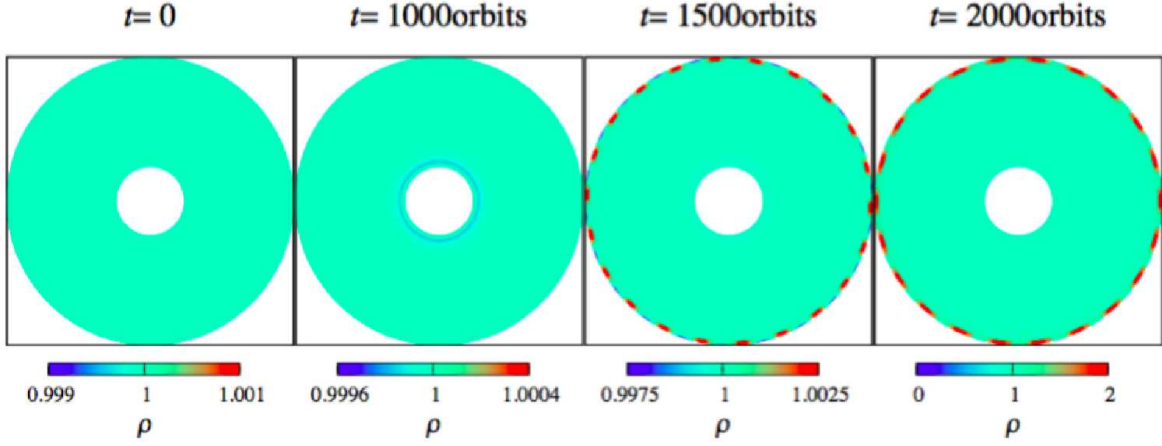


Fig. 33. The result of the cold Keplerian disk test. Density distributions at $t \simeq 0, 1000, 1500$ and 2000 orbits from left to right.

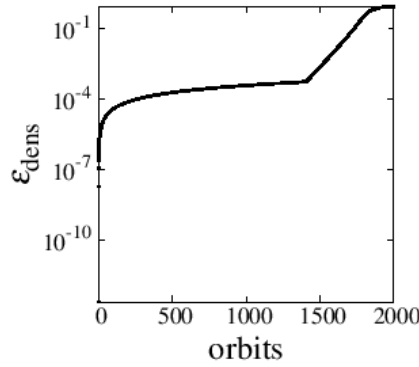


Fig. 34. The maximum error of density in particles plotted against the number of orbits in the cold Keplerian disk test.

4 Discussion and summary

4.1 Discussion

One limitation of our current CPHSF scheme is that there is no easy way to handle topological changes of fluid, for example the collision of two droplets. In principle, we can handle collisions by detecting the moment of the collision and change the surface particles (usually with special boundary conditions) to bulk particles. However, finding the exact moment of collision for each of surface particles involved can be very expensive. Therefore approximate treatment is practically necessary. Another problem is that we currently need implicit time integration in order to apply boundary conditions. An explicit or semi-implicit scheme would be better, and should be applicable at least to the bulk of the fluid.

4.2 Summary

Standard SPH scheme and its variations are not high order and cannot handle free surfaces. We formulate CPHS, a high-order mesh-free method. CPHSF can handle Kelvin-Helmholtz instability and Rayleigh-Taylor instability better than previous SPH methods do. We also simulate the gravity wave and dam break. The results are excellent. Additionally, the cold Keplerian disk, which is very important in astrophysics, can be calculated for much larger time than possible with previous mesh-free methods.

CPHSF does not exactly satisfy the conservation laws. However we showed that the violation of the conservation laws is acceptable, because of the Lagrangian nature and high-order accuracy of CPHSF. Therefore we conclude that CPHSF is more useful than previous mesh-free method.

Acknowledgments

We thanks Takayuki Saitoh for discussion about mesh-free method and others, Natsuki Hosono, Masaki Iwasawa and many others for providing useful comments about numerical simulations, Keigo Nitadori for discussion about formulation. We thank the referee for insightful and helpful comments. This work was supported by RIKEN Junior Research Associate Program and MEXT SPIRE and JICFuS. Part of the research covered in this paper was funded by MEXT's program for the Development and Improvement for the Next Generation Ultra High-Speed Computer System, under its Subsidies for Operating the Specific Advanced Large Research Facilities.

References

- Agertz, O., Moore, B., Stadel, J., et al. 2007, MNRAS, 380, 963
- Antuono, M., Colagrossi, A., Marrone, S., & Lugni, C. 2011, Computer Physics Communications, 182, 866
- Balsara, D. S. 1995, Journal of Computational Physics, 121, 357
- Bilotta, G., Russo, G., H erault, A., & Del Negro, C. 2011, Annals of Geophysics, 54
- Chen, J., Beraun, J., & Jih, C. 1999a Computational Mechanics, 23, 279
- Chen, J., Beraun, J., & Jih, C. 1999b Computational Mechanics, 24, 273
- Chen, J., Beraun, J., & Carney, T. 1999c International Journal for Numerical Methods in Engineering, 46, 231.
- Chen, J., & Beraun, J. 2000 Computer Methods in Applied Mechanics and Engineering, 190, 225
- Chock, David P. 1991, Atmospheric Environment. Part A. General Topics, 25, 853
- Crowley, Wp. 1968, Monthly Weather Review, 96, 1
- Cullen, L., & Dehnen, W. 2010, MNRAS, 408, 669
- Dilts, G. A. 1999, International Journal for Numerical Methods in Engineering, 44, 1115
- Fang, J., Parriaux, A., Rentschler, M., & Ancy, C., 2009 Applied Numerical Mathematics 59, 251.

Frontiere, N., Raskin, C. D., & Owen, J. M. 2016, arXiv:1605.00725

Gingold, R. A., & Monaghan, J. J. 1977, MNRAS, 181, 375

Hernquist, L., & Katz, N. 1989, ApJS, 70, 419

Hopkins, P. F. 2015, MNRAS, 450, 53

Hosono, N., Saitoh, T. R., & Makino, J. 2016, ApJS, 224, 32

Imaeda, Y., & Inutsuka, S.-i. 2002, ApJ, 569, 501

Inutsuka, S.-I. 2002, Journal of Computational Physics, 179, 238

Koshizuka, S., & Oka, Y. 1996, Nuclear Science Engineering, 123

Lattanzio, J. C., Monaghan, J. J., Pongracic, H., & Schwarz, M. P. 1985, MNRAS, 215, 125

Lax, P. D., & Richtmyer, R. D. 1956 Communications on pure and applied mathematics, 9, 267.

Liu, W. K., Jun, S., & Zhang, Y. F. 1995 International journal for numerical methods in fluids, 20, 1081.

Liu, M., Xie, W., & Liu, G. 2005 Applied mathematical modelling, 29, 1252.

Lobovský, L., Botia-Vera, E., Castellana, F., Mas-Soler, J., & Souto-Iglesias, A. 2014, Journal of Fluids and Structures, 48, 407

Lucy, L. B. 1977, AJ, 82, 1013

Martin, J. C., & Moyce, W. J. 1952, Philosophical Transactions of the Royal Society of London Series A, 244, 312

McNally, C. P., Lyra, W., & Passy, J.-C. 2012, ApJS, 201, 18

Monaghan, J. J. 1994, Journal of Computational Physics, 110, 399

Monaghan, J. J. 1997, Journal of Computational Physics, 136, 298

Monaghan, J. J., & Gingold, R. A. 1983, Journal of Computational Physics, 52, 374

Morris, J. P., & Monaghan, J. J. 1997, Journal of Computational Physics, 136, 41

Okamoto, T., Jenkins, A., Eke, V. R., Quilis, V., & Frenk, C. S. 2003, MNRAS, 345, 429

Ott, F., & Schnetter, E. 2003, arXiv:physics/0303112

Price, D. J. 2008, Journal of Computational Physics, 227, 10040

Ritchie, B. W., & Thomas, P. A. 2001, MNRAS, 323, 743

Rosswog, S., Davies, M. B., Thielemann, F.-K., & Piran, T. 2000, A&A, 360, 171

Saitoh, T. R., & Makino, J. 2013, ApJ, 768, 44

Sod, G.A. 1978, Journal of computational physics, 27, 1

Staroszczyk, R. 2010, Archives of Hydro-Engineering and Environmental Mechanics, 57, 61.

Tamai, T., Shibata, K., & Koshizuka, S. 2013 Trans. JSCES

Vijay, K. 1998, Applied Computational Fluid Dynamics, (United States: CRC Press), 1

Von Neumann, J., & Richtmyer, R. D. 1950, Journal of Applied Physics, 21, 232

Wendland, H. 1995, Advances in computational Mathematics, 4, 389.

- Whitham, G. 1999, *Linear and Nonlinear Waves*, ed. Allen III, M. B., Cox, D.A., Lax, P., Toland, J., (State of New Jersey: Wiley-Interscience), 1
- Yamamoto, S., Saitoh, T. R., & Makino, J. 2015, *PASJ*, 67, 37
- Yamartino, R.J. 1993, *Monthly Weather Review*, 121, 753
- Zhang, G., & Batra, R. 2004, *Computational Mechanics*, 34, 137.